Nano-Micro Letters
e-ISSN 2150-5551
CN 31-2103/TB
ARTICLE

Cite as
Nano-Micro Lett.
(2025) 18:94

Received: 23 April 2025
Accepted: 23 August 2025
Published online: 2 January 2026

Achieving Wide-Temperature-Range Physical and Chemical Hydrogen Sorption in a Structural Optimized Mg/N-Doped Porous Carbon Nanocomposite

Yinghui Li[1,2], Li Ren[1,2], Zi Li[1,2], Yingying Yao[1,2], Xi Lin[1], Wenjiang Ding[1,2], Andrea C. Ferrari[3] ✉, Jianxin Zou[1,2,3] ✉

HIGHLIGHTS

- The as-synthesized rN-pC exhibited H_2 uptake of ~0.9 wt% at 77 K and ultralow pressure of ~0.1 bar, with an isosteric adsorption enthalpy (Q_{st}) of ~14 kJ mol^{-1} H_2 at zero coverage.
- The 60MgH_2@rN-pC started to decompose at 175 °C and released H_2 of 3.38 wt% at 300 °C within 30 min, which showed outstanding desorption kinetics of MgH_2 among Mg-carbon material nanocomposites.
- The drawback of nanoconfinement scaffolds that cannot store hydrogen was firstly overcome.

ABSTRACT Nanoconfinement is a promising approach to simultaneously enhance the thermodynamics, kinetics, and cycling stability of hydrogen storage materials. The introduction of supporting scaffolds usually causes a reduction in the total hydrogen storage capacity due to "dead weight." Here, we synthesize an optimized N-doped porous carbon (rN-pC) without heavy metal as supporting scaffold to confine Mg/MgH_2 nanoparticles (Mg/MgH_2@rN-pC). rN-pC with 60 wt% loading capacity of Mg (denoted as 60 Mg@rN-pC) can adsorb and desorb 0.62 wt% H_2 on the rN-pC scaffold. The nanoconfined MgH_2 can be chemically dehydrided at 175 °C, providing ~ 3.59 wt% H_2 with fast kinetics (fully dehydrogenated at 300 °C within 15 min). This study presents the first realization of nanoconfined Mg-based system with adsorption-active scaffolds. Besides, the nanoconfined MgH_2 formation enthalpy is reduced to ~ 68 kJ mol^{-1} H_2 from ~ 75 kJ mol^{-1} H_2 for pure MgH_2. The composite can be also compressed to nanostructured pellets, with volumetric H_2 density reaching 33.4 g L^{-1} after 500 MPa compression pressure, which surpasses the 24 g L^{-1} volumetric capacity of 350 bar compressed H_2. Our approach can be implemented to the design of hybrid H_2 storage materials with enhanced capacity and desorption rate.

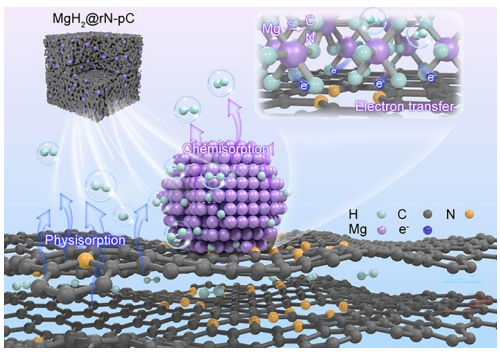

KEYWORDS Hydrogen storage; MgH_2; Porous carbon; Nanoconfinement; Physi- and chemisorption

✉ Andrea C. Ferrari, acf26@eng.cam.ac.uk; Jianxin Zou, zoujx@sjtu.edu.cn
[1] Shanghai Key Laboratory of Hydrogen Science & Center of Hydrogen Science, Shanghai Jiao Tong University, Shanghai 200240, People's Republic of China
[2] National Engineering Research Center of Light Alloys Net Forming & State Key Laboratory of Metal Matrix Composites, Shanghai Jiao Tong University, Shanghai 200240, People's Republic of China
[3] Cambridge Graphene Centre, University of Cambridge, Cambridge CB3 0FA, UK

1 Introduction

Clean and renewable energy is vital for sustainable development [1]. Hydrogen has high gravimetric energy density (lower heating value (LHV) ~ 120 MJ kg^{-1}) [2] and zero carbon emission (only water as combustion product) [3], making it promising as energy carrier. However, the large-scale application of H_2 as energy carrier is still hampered by the difficulties of effective storage [4]. Compared with storing H_2 as a compressed gas at high pressures up to 70 MPa [5], or as a liquid at cryogenic temperatures (T = 20 K) [6], solid-state H_2 storage has the advantages of mild operation conditions (lower than 10 Mpa working pressure [7] and higher than 77 K working T [8] for storage and transportation) and reduced cost of storage systems. Due to the high gravimetric and volumetric H_2 storage density (~ 7.6 wt% H_2 and ~ 110 kg m^{-3} H_2, respectively) [9], complete heat-driven reversible transformation ($MgH_2 \rightleftharpoons Mg + H_2$) [10], and earth-abundant natural Mg containing minerals such as dolomite [11] and seawater [12], MgH_2 is one of the most promising candidates for solid-state H_2 storage [13]. Nonetheless, the high thermodynamic stability and kinetic reaction barriers (ΔH = ~ 75 kJ mol^{-1} H_2, and ΔE = ~ 160 kJ mol^{-1} H_2, respectively) [14] limit its industrial application. Zhang et al. studied the solar-driven reversible hydrogen storage of MgH_2 and utilized solar energy as the sustainable energy source to reduce the energy costs [15, 16]. Besides, different approaches have been proposed to improve the thermodynamic and kinetic properties of MgH_2, including alloying [17], catalysts doping [18], and nanostructuring [19].

Nanostructuring (reducing particle size to the nanoscale or confining of nanoparticles (NPs) in supporting materials) of MgH_2 is a promising approach to enhance its thermodynamic and kinetic performances simultaneously [20], since this results in heterostructured interfaces with enhanced energy, shortened H diffusion pathways, and increased active sites [21]. Nanoconfinement of Mg/MgH_2 NPs in porous supporting scaffolds is an effective way to synthesize nano-sized Mg-based H_2 storage materials [22]. The porous supporting materials could prevent Mg/MgH_2 NPs aggregation and growth during thermal-induced de/re-hydrogenation cycles, usual for free-standing nanostructured Mg/MgH_2 [23]. An excellent supporting scaffold should have chemical inert (stability under operation T and H_2 atmosphere), light weight (low volumetric density) and catalytic activity for the H_2 ab/desorption process. Carbon-based materials, such as graphene [24], carbon aerogels [25], ordered mesoporous carbon (CMK3) [26] et al. have been used as supporting materials to confine MgH_2 NPs. Xia et al. prepared monodisperse MgH_2 NPs self-assembled on Ni-modified graphene with multilayer synthesized through chemical intercalation of graphite. Hydrogenated composites could realize complete dehydrogenation at 200 °C within 150 min [24]. Jensen et al. synthesized nanoporous carbon aerogel scaffolds X1 and X2, with average pore sizes of 22 and 7 nm, and the dehydrogenation kinetics of the confined hydride in smaller pores was faster due to the size reduction [25]. However, these carbon-based materials show no catalytic activity [27], and additional metal catalysts, such as Fe, Co, Ni [28, 29], are needed to improve the H_2 storage performance. The loading of MgH_2 is limited by the scaffolds' structure [25], and the synthesis routes [30]. Pore blocking was found in oxygen-containing carbons, and bulk Mg was detected in the samples with Mg loadings > 15 wt% [31], indicating loading should be selected considering the compromise between capacity and desorption T [32]. Besides, the introduction of a scaffold without H_2 storage capacity leads to the loss of total H_2 storage capacity. It is thus necessary to prepare a scaffold with self-adsorbing H_2 capacity for nanoconfinement of Mg/MgH_2 NPs, so as to improve the Mg-based H_2 storage performance and introduce extra physical H_2 adsorption capacity.

The development of high-pressure and cryogenic technologies (with controllable operation over 10 MPa at −196 °C) [33] enables the exploration of new adsorbent materials, such as metal organic frameworks (MOFs) [34], covalent organic frameworks (COFs) [35], and porous carbons (pCs) [36], as other promising strategies to realize safe and cost-effective H_2 storage. Among them, porous carbons have the advantages of easy synthesis, thermal and chemical stability, and tuneable porosity, as well as being suitable confinement scaffolds for Mg/MgH_2 [37].

Here, we synthesize an ammonia (NH_3)-optimized N-doped porous carbon (rN-pC) with reversible H_2 adsorption capacity to confine MgH_2. For H_2 adsorption a high zero coverage adsorption heat (= 14 kJ mol^{-1} H_2) was achieved, leading to adsorption capacity close to 1% at a pressure as low as 0.01 Mpa. Mg NPs form on rN-pC to obtain a 60 Mg@rN-pC composite through nanoconfinement. N-doped carbon facilitates electron transfer from MgH_2 to the scaffold, weakening the

https://doi.org/10.1007/s40820-025-01931-w

Mg–H bonds and decreasing the operation T for dehydrogenation. 60MgH_2@rN-pC shows low onset desorption temperature (T_{onset}, 175 °C) and 10-cycling H_2 absorption and desorption stability, presenting outstanding catalytic effects when compared to state-of-art non-metal catalyzed MgH_2 systems [38]. 60MgH_2@rN-pC composites can deliver 4.2 wt% H_2 within two T ranges (physical desorption from -196 °C and chemical desorption from 175 °C). As T increases, the H_2 stored in the micropores of scaffold (N–pC) by physical adsorption at −196 °C is preferentially released, followed by further release of H_2 stored in MgH_2 via chemisorption. Thus, our synergistic approach yields a hybrid H_2 storage composite material, with both physical and chemical H_2 sorption ability, enabling a new strategy to develop advanced energy storage materials.

2 Experimental Section

2.1 Materials

Zinc nitrate hexahydrate ($Zn(NO_3)0.6H_2O$ 98%) was purchased from Thermo Fisher Scientific Inc. (USA). 2-methylimidazole (2-Hmim98%) and methanol were supplied by Shanghai Aladdin Biochemical Technology Co., Ltd. (China). Anhydrous tetrahydrofuran (THF, 99.5%) was purchased from Tokyo Chemical Industry (TCI, Japan). Methyl magnesium chloride (CH_3MgCl, 3 M solution in anhydrous THF) and lithium foil (Li, 99.9%) were purchased from Sigma-Aldrich Lab (USA). Naphthalene ($C_{10}H_8$, > 99.7%,) was supplied by Shanghai Macklin Biochemical Co., Ltd. (China).

2.2 Synthesis of rN-pC Scaffolds

2.2.1 Synthesis of rN-pC Scaffolds

2.97 g $Zn(NO_3)0.6H_2O$ and 6.57 g 2-Hmim are dissolved in 200 mL of methanol, respectively. These two solutions are mixed and agitatedly stirred (500 rpm) for 10 min, followed by standing for 24 h at room temperature (RT). The resultant white precipitation is centrifuged and washed 3 times with methanol, and dried in an oven at 60 °C overnight to obtain ZIF-8 NPs. ZIF-8 is heated to 1000 °C with a ramp of 10 °C min^{-1} under Ar/5% H_2 and kept at 1000 °C for 30 min (denoted as N-pC), followed by NH_3 treatment at 750 °C for 30 min. rN-pC is obtained after cooling to RT.

2.2.2 Synthesis of 60MgH_2@rN-pC

All samples are prepared in an inert atmosphere (Ar-filled glove box, Mikrouna). 60MgH_2@rN-pC is synthesized by a reduction reaction of in situ grown Mg NPs on rN-pC. CH_3MgCl, Li foil, $C_{10}H_8$ and anhydrous THF are used as received without further treatment. 30 mg as-prepared rN-pC was processed in 20 mL THF under intermittent ultrasonication for 1 h, and then 0.6 mL CH_3MgCl was added for another 1 h intermittent sonication (200 W for 2 h, 15 s pulse and 15 s relaxation) (solution A). 31.23 mg Li foil and 615.26 mg naphthalene were dissolved in 30 mL THF with rapid stirring (800 rpm) for 3 h (solution B). Then, solution A was dripped dropwise into solution B and stirred for 2 h at RT. 0.6 mL of CH_3MgCl (1.8 mmol) can be reduced to get 43.2 mg Mg and hydrogenated to obtain 46.8 mg MgH_2. Therefore, the weight percent of MgH_2 in the 60MgH_2@rN-pC composite is calculated to be ~ 60 wt% (46.8/76.8 mg). The 60 Mg@rN-pC composite is derived from the desorption of 60MgH_2@rN-pC. The resultants were centrifugated and washed 3 times with THF. Finally, the participants were dried under vacuum in the glove box and hydrogenated to obtain 60MgH_2/rN-pC. Pure Mg/MgH_2 were synthesized with the same steps without adding rN-pC. In the present research, 60MgH_2@rN-pC-as synthesis/absorption/desorption belong to different states of one sample.

2.3 Materials Characterization

Specific surface area (SSA) and pore size distribution (PSD) are estimated via N_2 ad/desorption tests at −196 °C on a Autosorb-IQ3 apparatus (Quantachrome). The phase composition is analyzed by X-ray diffraction (XRD, Mini Flex 600, Rigaku, Cu Kα) at 40 kV/15 mA with a scanning speed of 10° min^{-1}. The samples are prepared in an Ar-filled glovebox and sealed in a custom-designed holder covered by an amorphous tape to avoid air exposure during testing. (High-resolution) Transmission electron microscopy ((HR)TEM) and selected area electron diffraction (SAED) are performed on a Talos F200X G2 microscope with an accelerating voltage of 200 kV. The samples were ultrasonically dispersed in tetrahydrofuran (THF), and then, in a glovebox, the dispersion liquid was dropped on a copper grid, which was sealed and transferred to the TEM

instrument rapidly. The morphologies of products are also examined by scanning electron microscopy (SEM, Mira3 and Rise-magna, TESCAN). An air-proof transfer vessel is used to transfer the samples from glovebox to X-ray photoelectron spectroscopy equipment (XPS, Kratos AXIS Ultra DLD, Al Kα/Mg Kα) to characterize the elemental valence and chemical bonding. For the XPS analysis of powder samples, the following preparation procedures were employed: In an argon-filled glovebox, a minimal amount of sample was transferred onto conductive carbon tape mounted on the sample holder using a toothpick, followed by flattening the surface with a spatula. The whole sample stage was sealed in the air-proof transfer vessel, which would be connected with the testing instrument directly. For the XPS measurements, monochromatic X-ray of Al Kα (~ 1487 eV) was used to induce the generation of photoelectrons. For the comparison of one element in different samples, the same testing parameters (working steps, dwell times, etc.) were used to minimize systematic errors. The C–C binding energy at 284.8 eV is used to calibrate the XPS data [39]. Raman spectra are collected using micro-Raman spectroscopy from Renishaw inVia Qontor with 532 nm lines and from Horiba LabRAM HR Evolution, Horiba Scientific with 325, 514, and 633 nm. FTIR spectra in transmittance mode are measured with a Thermo Scientific Nicolet iS5. DSC curves are obtained on a NETZSCH STA449F3 Jupiter facility under flowing Ar. The measurements were conducted by heating the samples from room temperature to 500 °C with the heating rates of 3, 5, 7, and 10 °C min^{-1}. Thus, the testing duration varies with the heating rate, which is 158.3, 95, 67.8, and 47.5 min, for the heating rates of 3, 5, 7, and 10 °C min^{-1}, respectively. Around 5–10 mg sample was used for each test. Activation energy (E_a) is obtained by fitting DSC data using the Kissinger method. The isothermal ad/ab/desorption tests and TPD measurements are carried out in a Sievert-type pressure-composition-T apparatus (PCT, HPSA-auto device, China), in which the modified Benedict–Webb–Rubin (MBWR) [40] equation of state (EOS) is used to calculate H_2 storage capacity. −196/−186 °C isothermal volumetric H_2 adsorption tests are done at liquid N_2 and Ar, respectively. Before the physical adsorption measurements, all samples are outgassed at 300 °C for 12 h, and then the Mg is fully adsorbed at 300 °C. Subsequently, the samples are cooled down to room temperature under certain H_2 back pressure and then degassed in vacuum for another 1 h. Typically, for the isothermal ab/desorption tests, ~ 100 mg is loaded into the test tube in a glove box and heated to the preset T by rapid heating rate (~ 5–10 °C min^{-1}), then maintaining this T during the thermodynamic test. The H_2 ab/desorption kinetics is measured at various T for an initial H_2 pressure of 3 MPa for absorption and 0.001 MPa for desorption, respectively. The hydrogenated samples are heated from RT to 350 °C with a heating rate ~ 2 °C min^{-1} under a primary vacuum to conduct TPD measurements. The H_2 pressure/duration/T parameters of pure Mg used for cycling tests are set as 3 MPa/20 min/350 °C for re-hydrogenation and 0.03 MPa/45 min/350 °C for dehydrogenation. For 60MgH_2/rN-pC those are set to 3 MPa/15 min/275 °C for re-hydrogenation and 0.03 MPa/60 min/275 °C for dehydrogenation. H_2 storage capacity is calculated as wt% of entire composite including rN-pC scaffold. The compression machine is a PC-12 type tablet press from Tianjin Jingtuo Company. A cylindrical die with the inner diameter 10 mm was used to prepare the composite pellets and the effective pressure on the pellets was set at ~ 500 MPa (4 Tons).

2.4 Density Functional Theory Calculations

Density functional theory (DFT) calculations are performed using quantum espresso (QE) based on the pseudopotential plane wave (PPW) method [41]. Perdew–Burke–Ernzerhof (PBE) functionals [42] are used to describe exchange–correlation effects of electrons. The projected augmented wave (PAW) potentials [43] are used to describe the ionic cores and take valence electrons into account using a plane wave basis set with a kinetic energy cutoff = 500 eV. All structures are first optimized to reach their most stable configuration. During geometry optimization, all atom positions are allowed to relax. Brillouin-zone sampling is conducted using a Monkhorst–Pack (MP) [44] grid with separation of 0.04 $Å^{-1}$. The convergence criterion for the electronic self-consistent field (SCF) loop is set to 1×10^{-5} eV $atom^{-1}$ to ensure accurate total energy calculations while maintaining computational efficiency [45]. The atomic structures are optimized until the residual forces are < 0.05 eV $Å^{-1}$. The adsorption energies between porous carbon substrates and H_2 are computed as [46]:

https://doi.org/10.1007/s40820-025-01931-w

$E_{ad} = E_{sub-H2} - E_{sub} - E_{H2}$,

The differential charge density is calculated as [46]: $\Delta\rho = \rho_{tot} - \rho_{sub} - \rho_{abs}$.

where ρ_{tot}, ρ_{sub} and ρ_{abs} represent the total charge density, charge density of substrate and charge density of absorbed molecules.

3 Results and Discussion

3.1 Preparation and Characterization of rN-pC

MOFs have high SSA from hundreds to thousands $m^2\ g^{-1}$ [47, 48], but relatively poor thermal stability compared with zeolites [49] and carbons [50], so their degassing pre-activation is difficult and sensitive to T control. The thermal stability of carbon materials derived from MOFs has improved with the decomposition and carbonization of ligands [51], but their SSA has reduced due to the collapse of the ordered three-dimensional structures during heat treatment [52]. NH_3 etching of the carbon matrix leads the formation of pores, as well as the introduction of active N atoms, favorable for H_2 adsorption [53]. Here, we prepared N-doped porous carbon (N-pC) from zeolitic imidazolate frameworks (ZIF-8) by heat treatment. Its structure and composition are optimized by NH_3 treatment to enrich N doping porous carbon (rN-pC) (Fig. S1).

The crystal structures, pore distributions and heteroatoms are systematically characterized. X-ray diffraction (XRD) patterns in Fig. S2a of the as-synthesized ZIF-8 match the simulated XRD standard pattern and those reported in literatures [54, 55]. After pyrolysis of ZIF-8 at 1000 °C, the resulting N-pC displays two humps at ~ 23.8° and 43.3°, implying its deficiency of periodic graphitic structure (full width at half maximum of (FWHM) (002) diffraction peak of ~ 12°) [56], while NH_3 has little effect on the crystal structure (Fig. S2a). However, as shown in Figs. 1a, S2b and Table S1, the SSA, PSD, and pore volume (PV) of N-pC change after NH_3 treatment. Brunauer–Emmett–Teller (BET) tests in Fig. 1a show SSA and PV of ZIF-8 ~ 1877 $m^2\ g^{-1}$ and 0.71 $cm^3\ g^{-1}$, much higher than N-pC (925.8 $m^2\ g^{-1}$ and 0.92 $cm^3\ g^{-1}$) owing to the structural collapse during pyrolysis. Correspondingly, N-pC has a type-IV isotherm [57], with an adsorption–desorption hysteresis loop at the relative pressure p/p_0 of 0.5–1, suggesting the generation of mesopores (2–50 nm) [58], suitable for the impregnation of organic Mg precursors. SSA and PV of rN-pC increase to 1525.4 $m^2\ g^{-1}$ and 1.50 $cm^3\ g^{-1}$, mainly due to NH_3 etching, thus achieving pore enlargement [59]. PSD plots are obtained using the Barrett–Joyner–Halenda (BJH) method to analyze the pore structure of N-pC and rN-pC (Fig. S2b). N-pC and rN-pC possess hierarchically porous architecture with additional mesopores compared with monosized microporous ZIF-8, while the pore structure changes from micro to meso.

Chemical compositions and elemental valence states are investigated by X-ray photoelectron spectroscopy (XPS) (Figs. 1b and S2c). XPS spectra of N-pC and rN-pC show three dominant peaks at 288, 399, and 532 eV, assigned to C 1*s*, N 1*s*, and O 1*s* [60]. The C 1*s* spectra are almost the same for both N-pC and rN-pC, and the high-resolution C 1s peak can be deconvoluted into C–C (284.8 eV), C-N/C-O (287.1 eV), and C = O (289.5 eV) groups [61]. The high-resolution N 1*s* XPS consists of 5 peaks with binding energies of 398.5, 399.7, 401.1, 402.9, and 405.0 eV, corresponding to pyridinic, pyrrolic, graphitic, quaternary, and oxidized N groups [59]. Compared with N-pC, rN-pC contains more pyridinic N groups, improving its electron-transferring ability [62]. From XPS (Table S2), the N content of rN-pC increases from 2.5 wt% to 6 wt%, suggesting the possible transformation of C = C to C-N during NH_3 treatment. The Raman spectra were measured under different excitation of 325, 514, 532, and 633 nm with a linear baseline subtraction and then deconvoluted to Gaussian lines. Considering of the amorphous structure and broadening D peaks, the ratio of peak areas was compared [63]. The signals of N-pC and rN-pC were detected at ~ 1360 cm^{-1} (D band) and ~ 1580 cm^{-1} (G band), usually involving in the in-plane bond-stretching motion of all pairs of sp^2 atoms and breathing mode of sp^2 atoms in rings [64], respectively. 514 nm Raman spectra in Fig. S2d show that N-pC has D peak at ~ 1359 and G peak at ~ 1584 cm^{-1}, with FWHM (G) = 91 cm^{-1} and I(D)/I(G) = 2.11, and rN-pC has D peak at ~ 1355 and G peak at ~ 1585 cm^{-1}, with FWHM (G) = 113 cm^{-1} and I(D)/I(G) = 2.66. After NH_3 treatment, the dilated G peak width and increasing values of I(D)/I(G) can be attributed to the N doping and activation of sixfold aromatic rings, as well as NH_3 etching and shrinking of ring clusters, which is coincident with the BET and XPS results [65]. The results under different excitation wavelength

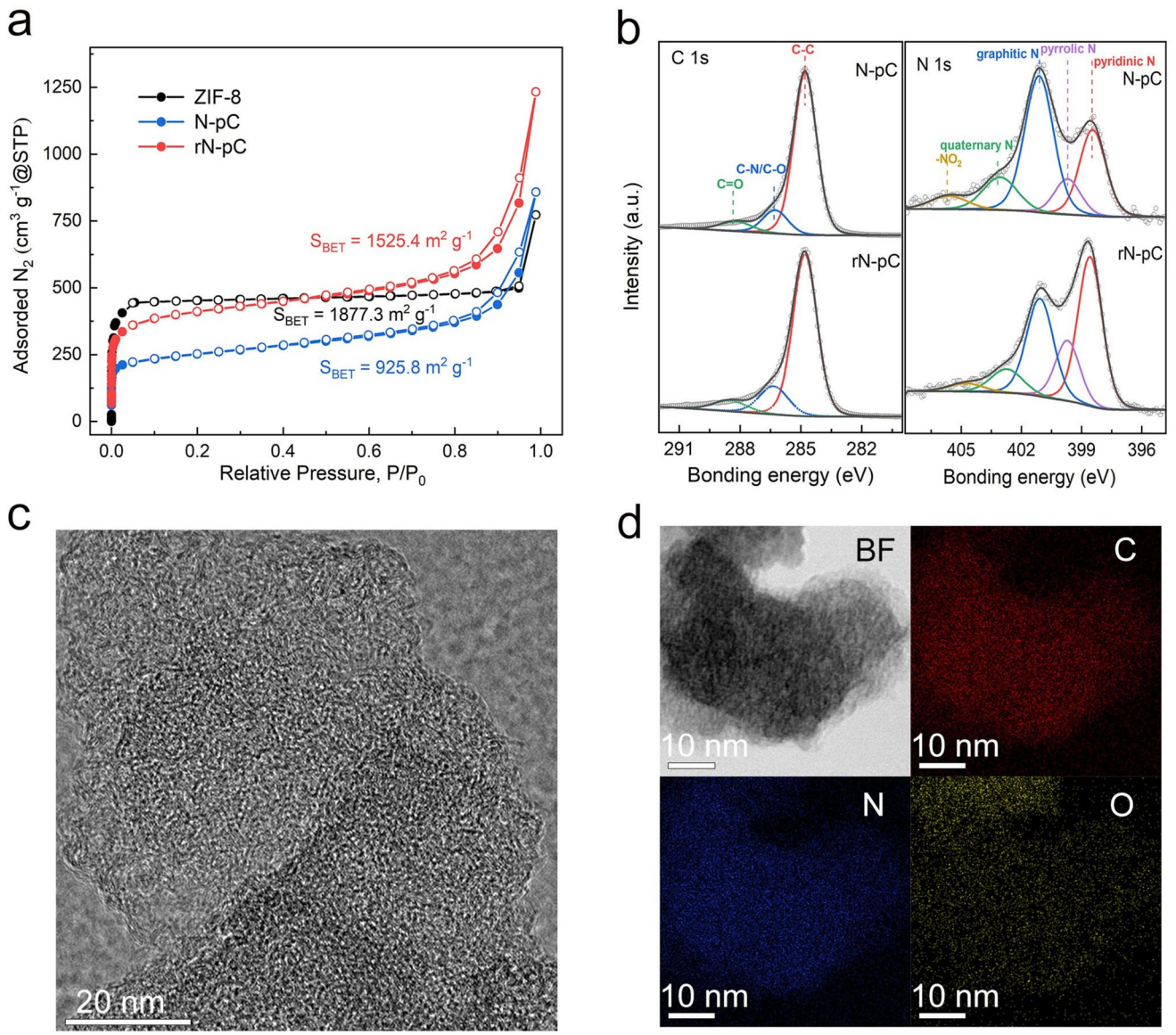

Fig. 1 Structure and morphology characterization of rN-pC. **a** N_2 adsorption/desorption isotherms, and **b** high-resolution XPS spectra of C 1*s* and N 1*s* of N-pC and rN-pC. **c** TEM image, **d** representative BF image and EDS elemental mappings of rN-pC

exhibit the same trend in FWHM (G) and I(D)/I(G), which are shown in Fig. S3a-d with error bars.

The microstructure and morphology of ZIF-8, N-pC and rN-pC are further characterized by scanning electron microscopy (SEM, Mira3, Fig. S4) and transmission electron microscopy (TEM, Talos F200X G2, Figs. 1c and S5). As prepared ZIF-8 shows a spherical structure with an average size ~ 30 nm. After heat treatment under Ar and NH_3. TEM shows a porous architecture within the N-pC skeleton, stemming from the evaporation of Zn accompanied by the collapse of ZIF-8 frameworks. This structure still remains porous after NH_3 treatment. The size of the N-pC or rN-pC is ~ tens nm due to different degrees of integration between ZIF frameworks. The representative HRTEM images in Figs. 1c and S4 demonstrate that N-pC and rN-pC have similar porous and nanocrystalline graphite structure with the existence of ~ 5 layered short domains. Scanning transmission electron microscopy (STEM, Talos F200X G2, Figs. 1d and S5d) mapping of N-pC and rN-pC shows a homogenous distribution of N in the porous matrix. The N content of rN-pC is higher than N-pC (Table S3), consistent with XPS (Table S2). The higher N content and the optimized porous

https://doi.org/10.1007/s40820-025-01931-w

structure endow rN-pC with more H_2 adsorption-active sites and surface hydrophilicity, facilitating the nucleation of Mg/MgH_2 NPs [66].

3.2 Hydrogen Adsorption Properties of rN-pC

The rN-pC has high SSA (1525.4 $m^2 g^{-1}$) and a certain number of micropores (0.447 mL g^{-1}), suggesting potential H_2 adsorption ability. The H_2 storage performance of rN-pC are evaluated through high-pressure (0–6 MPa) excess H_2 adsorption at –196 and –186 °C (Fig. 2a). These are modeled using a semi-empirical methodology (Eq. S1), then converted to absolute H_2 uptake.

Owing to the stability of rN-pC under 750 °C treatment, the pre-activating treatment can be executed under high T > 300 °C, without any changes of structure and constituents, so that the degassing procedure can be simplified. The gravimetric H_2 excess uptake of rN-pC increases abruptly and reaches a saturation plateau ~ 1 MPa (Fig. 2a), because N and micropores act as active adsorption sites for H_2 adsorption. With the PSD of 0.5–30 nm in rN-pC, the H_2 density adsorbed in mesopores is smaller than that in micropores. Therefore, a fast drop of excess adsorption is observed with increasing pressure, due to the gas density increasing with pressure faster outside than inside the pores [67]. Excess gravimetric H_2 uptake ~ 2.5 wt% at −196 °C and ~ 0.8 Mpa, and ~ 2.3 wt% at −186 °C and ~ 1.5 MPa is detected. The saturation plateau at −186 °C shifts to a higher position compared with that at −196 °C, due to the decrease in free gas density [68]. An absolute gravimetric H_2 uptake ~ 3.4 and ~ 3.0 wt% is recorded for rN-pC at ~ 6 MPa and −196 °C, −186 °C, respectively. The maximum volumetric H_2 uptake ~ 17.3 g H_2 L^{-1} is estimated considering the density functional theory (DFT, Equation S2) PV (~ 1.498 $cm^3 g^{-1}$) and the skeletal density (~ 2.15 g cm^{-3}) of rN-pC at −196 °C.

In order to investigate the interaction between H_2 and rN-pC, the ultralow pressure (below 0.01 MPa) H_2 adsorption isotherms at –196 and –186 °C are shown in Fig. S6. The gravimetric H_2 adsorptions at 0.01 MPa and −196/−186 °C are 0.9 and 0.55 wt%, respectively, meaning that rN-pC can reach a high H_2 adsorption under a low H_2 background pressure, indicating strong interaction compared with porous carbon [36]. The isosteric enthalpy of H_2 adsorption (Q_{st}), as derived by Langmuir fitting [69] of the ultralow pressure isotherms at −196 and −186 °C followed by a Clausius-Clapeyron calculation (Eq. S3) [70], is in Fig. 2b. The Q_{st} value at zero coverage is ~ 14 kJ mol^{-1}, much higher than classical H_2 physisorption (i.e., 1–10 kJ mol^{-1}). For most standard activated carbons, with the contribution of overlapping potential fields of opposite pore walls, the zero coverage isosteric adsorption enthalpy lies in the range ~ 5–10 kJ mol^{-1}, even if the binding strength of H_2 on carbon alone is weak (~ 1–5 kJ mol^{-1}) [71]. Q_{st} decreases with H_2 uptake to ~ 6 kJ mol^{-1} at 3 wt% adsorption, indicating the existence of favorable adsorption sites. We calculate the binding energies of H_2 on the different sites of N-doped C using DFT calculation. For H_2 interacting with carbon materials or graphitic/pyridinic N-doped carbon materials, a (4 × 4 × 1) supercell of carbon materials doped with N was primarily simulated, and the full optimized geometries are in Figs. 2c and S7, and the interaction energies in Fig. 2d. A stronger interaction is found when H_2 interacts with pyridinic N-doped carbon materials, with an enthalpy of 7.4 kJ mol^{-1} higher than that between H_2 and pure carbon materials (5.2 kJ mol^{-1}). Micropores with overlapping potential fields at opposite walls lead to stronger interaction between H_2 and substrate, but this is not taken into account in our calculations (details in Experimental Section), so that the experimental values are higher than the calculated values. The improvement of H_2 adsorption is confirmed by the density of state (DOS) and its projections for each atom and charge density difference (Figs. S8 and S9). With the contributions from N dopants, especially for pyridinic type, the DOS of substrates are closer to the Fermi level, stimulating stronger H_2 polarization and interactions [72]. Considering the high zero coverage Q_{st} (~ 14 kJ mol^{-1}) and high H_2 adsorption (0.9 wt% at -196 °C) under ultralow relative pressure ranges (< 0.1 bar) of rN-pC, Refs. [34, 62] suggested that H_2 adsorption of porous carbon depends on micropores, as well as its chemical composition [36, 73].

3.3 *Preparation and Structural Characterization of 60MgH_2@rN-pC*

60MgH_2@rN-pC is prepared via solution reduction of methyl magnesium chloride (CH_3MgCl) using lithium naphthalene (LiNaph), followed by hydrogenation. The porous

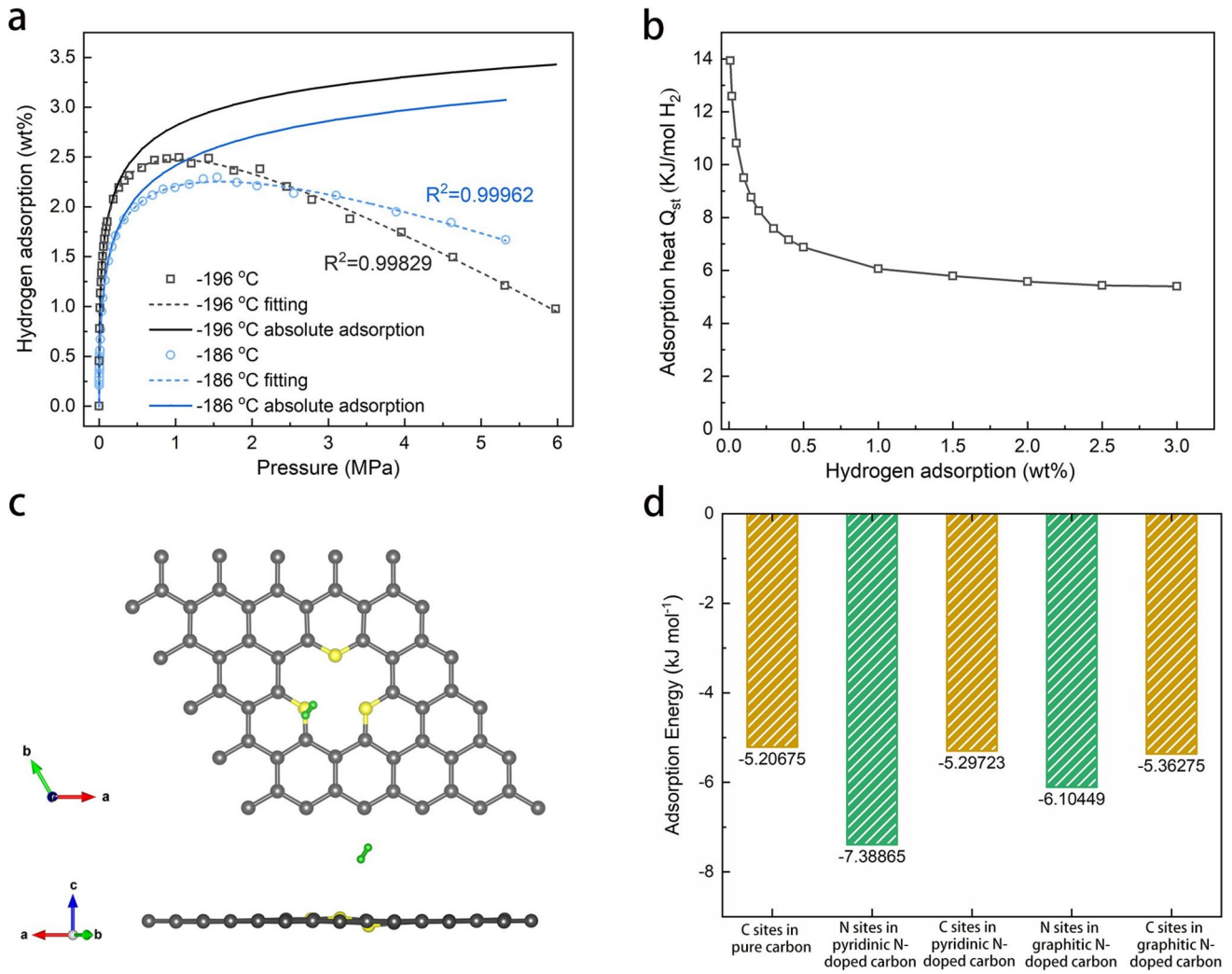

Fig. 2 Hydrogen adsorption properties of rN-pC at cryogenic T. **a** H_2 excess adsorption isotherms of rN-pC at -196, and -186 °C and corresponding modeling. **b** Equivalent isosteric heat of H_2 adsorption fitting of rN-pC. **c** Top and side views of optimized geometries of H_2 adsorbed on pyridinic N-doped graphene. **d** Adsorption energies for different substrate sites interacting with H_2

carbon confined Mg-based hydrogen storage composite was synthesized with robust interfaces and controllable structure through a simple and efficient method. To synthesize evenly distributed Mg NPs confined in rN-pC scaffolds, the mixture of rN-pC and CH_3MgCl is processed under intermittent ultrasonication to promote dispersion of rN-pC in tetrahydrofuran (THF), exposing free surfaces for impregnation of Mg.

Figure 3a shows low-magnification (5.8 k) TEM images of $60MgH_2$@rN-pC. The rN-pC scaffolds maintain a porous structure, and many MgH_2 NPs with uneven particles size homogenously distributed on the surface or in the open channel of the rN-pC (Fig. 3b, c). The absence of isolated MgH_2 NPs indicates coupling between Mg precursor and rN-pC substrates. Correspondingly, isolated Mg NPs > 300 nm were also synthesized under the same experimental conditions, except for the addition of rN-pC (Fig. S10). The redox reaction between CH_3MgCl and LiNaph takes place in seconds, and pre-dispersion and confinement of rN-pC is vital to obtain well-distributed Mg NPs. The microstructure of MgH_2@rN-pC is investigated by high-resolution TEM (HRTEM, Fig. 3b). The black NPs with an average size ~ 20 nm comprise more than ten MgH_2 grains with different orientations. The interplanar spacing ~ 0.225 nm

https://doi.org/10.1007/s40820-025-01931-w

corresponds to the (200) planes of MgH_2, while the interplanar spacing ~ 0.211 nm is assigned to the (200) planes of MgO [74]. The active MgH_2 NPs are oxidized by the residual moisture in the THF solvent and during the preparation and transportation before TEM measurement, consistent with the diffraction ring of MgO in the SAED pattern of Fig. S11. Figure 3c confirms that MgH_2 NPs < 5 nm are confined in the channel of rN-pC, as reported in literature [19], with outstanding H_2 thermodynamic and kinetic performances. Besides, the $60MgH_2$@rN-pC heterostructure still maintains its initial structure and shows no obvious agglomeration of MgH_2 after 10 cycles (Fig. S12). Fourier transform infrared (FTIR) spectra of rN-pC, pure MgH_2 and $60MgH_2$@rN-pC are also consistent with the introduction of MgH_2 NPs (Fig. S13). STEM mapping in Fig. 3d indicates homogeneous distribution of Mg, C, N in the MgH_2@rN-pC, in agreement with TEM. The BET and PSD analyses of rN-pC and $60MgH_2$@rN-pC based on DFT are in shown in Fig. S14. BET tests give a $60MgH_2$@rN-pC SSA ~ 636.5 $m^2 g^{-1}$, much lower than pristine rN-pC (1525.4 $m^2 g^{-1}$). The rN-pC PSD plot < 2.5 nm has a peak ~ 0.59 nm, not present for $60MgH_2$@rN-pC. This has 3 humps ~ 0.75, 1.3, and 1.6 nm, consistent with rN-pC, but with decreased average density. MgH_2 NPs are confined in the pore channel or cover the pore entrance, reducing SSA and the corresponding rN-pC pore size.

3.4 *H_2 Storage Properties of $60MgH_2$@rN-pC*

The H_2 hydrogen storage capacity of $60MgH_2$@rN-pC at cryogenic (–196 and –186 °C) and high T up to 350 °C was

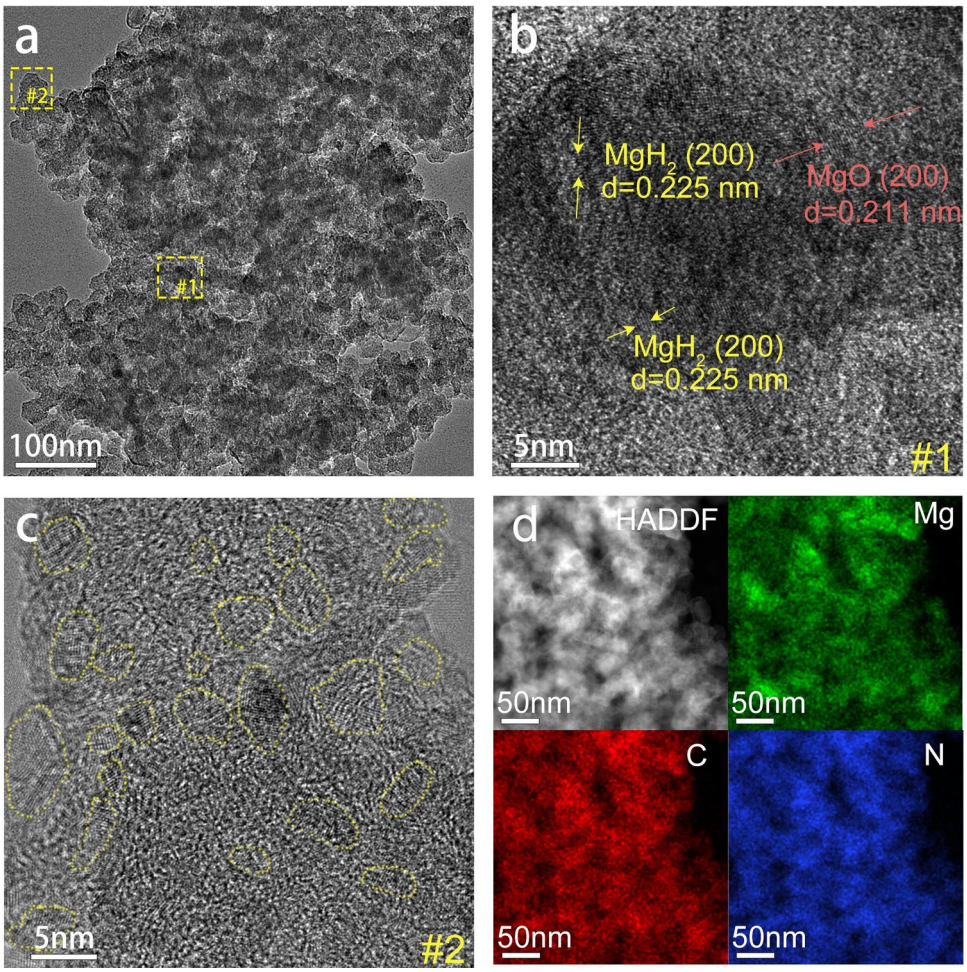

Fig. 3 Structure and morphology characterization of $60MgH_2$@rN-pC composite. **a** The TEM and **b, c** HRTEM images of hydrogenated $60MgH_2$@rN-pC. **d** HAADF image of $60MgH_2$@rN-pC and corresponding elemental mapping for Mg, C, N

tested. The data about physical adsorption of the composites were all collected in the state that Mg was fully hydrogenated. First, the gravimetric H_2 excess uptake of $60MgH_2$@rN-pC is measured at –196 °C. As for Fig. 4a, the H_2 excess adsorption content decreases to 0.66 wt% (2.5 wt% for rN-pC) and the adsorption saturation pressure shifts to higher value (~ 1 Mpa for rN-pC and ~ 1.8 Mpa for $60MgH_2$@rN-pC). The isosteric enthalpy of H_2 adsorption (Q_{st}) is calculated by Langmuir fitting of the ultralow pressure isotherms at –196 and –186 °C (Fig. S15). The zero coverage Q_{st} is estimated to be ~ 10.6 kJ mol^{-1}, in the range reported in literatures for H_2 physisorption [75]. A possible reason for the decrease of H_2 adsorption capacity and lowering of zero coverage Q_{st} could be related to the filling and coverage of pores by MgH_2 NPs, resulting in the reduction of effective contacts between H_2 and C, as well as active N sites. However, micropores in the carbon scaffold are less accessible for Mg precursors [76], which means that most nucleates on the mesopores and surfaces and partial micropores are retained. From the semi-empirical calculations described in Eq. S1, the H_2 adsorption density is ~ 0.045 g cm^{-3} (Table S4, 0.026 g cm^{-3} for rN-pC), indicating that it is possible to obtain an improved volumetric H_2 storage system. The H_2 cycling ad/desorption performance of $60MgH_2$@rN-pC is measured at -196 °C. As shown in Fig. 4b, H_2 adsorption is totally reversible, with no hysteresis. The excellent cycling stability indicates that $60MgH_2$@rN-pC maintains a stable porous structure and MgH_2 NPs are well bound to the rN-pC framework, without significant detachment under cryogenic T. This study shows the first realization of nanoconfined Mg-based system with adsorption-active scaffolds (Table 1).

We then study the high T (0–350 °C) H_2 storage properties of the pure MgH_2 and $60MgH_2$@rN-pC by T Programmed Desorption (TPD) analysis of $60MgH_2$@rN-pC in comparison with pure MgH_2 is in Fig. 5a. The samples for TPD analysis were obtained after initial hydrogenation. Pure MgH_2 starts to desorb H_2 at ~ 299 °C with a final capacity ~ 6.8 wt%. The T_{onset} of $60MgH_2$@rN-pC reduces to 175 °C, with a final capacity of 3.85 wt%. A small amount of Mg/MgH_2 reacted irreversibly with impurities in the chemicals to form MgO, leading to the capacity loss. ~ 3 wt% H_2 is released from $60MgH_2$@rN-pC before 300 °C, while pure MgH_2 starts to decompose at the same T. Differential scanning calorimetry (DSC) experiments are then performed at different heating rates ~ 3, 5, 7, 10 °C min^{-1} to further demonstrate the improvement of desorption properties (Fig. 5b). The peak desorption T of $60MgH_2$@rN-pC is 295.6 °C at the heating rate of 3 °C min^{-1}, 82.7 °C lower than that pure MgH_2 (378.3 °C) (Fig. S16). The apparent activation energy of desorption (E_a) is calculated from the Kissinger's equation (Eq. S4) [77]. Figures 5b and S16 show a linear relation between $\ln(\beta/T_p^2)$ and $1000/T_p$ (β represents the heating rate, Tp refers to the peak temperature) for $60MgH_2$@rN-pC and MgH_2. E_a of $60MgH_2$@rN-pC is fitted to ~ 142.1 ± 5.6 kJ mol^{-1} H_2, much lower than pure MgH_2 (189.2 ± 12.8 kJ mol^{-1} H_2), consistent with the calculation using the Johnson–Mehl–Avrami–Kolmogorov (JMAK) and Arrhenius equation [78] (Fig. S17, 148.2 ± 3.3 kJ mol^{-1} H_2 and 181.6 ± 0.8 kJ mol^{-1} H_2 for $60MgH_2$@rN-pC and pure MgH_2, respectively). The high desorption activation energy of pure MgH_2 comes from its surface structure with good crystallinity, as shown in Fig. S10, which is close to

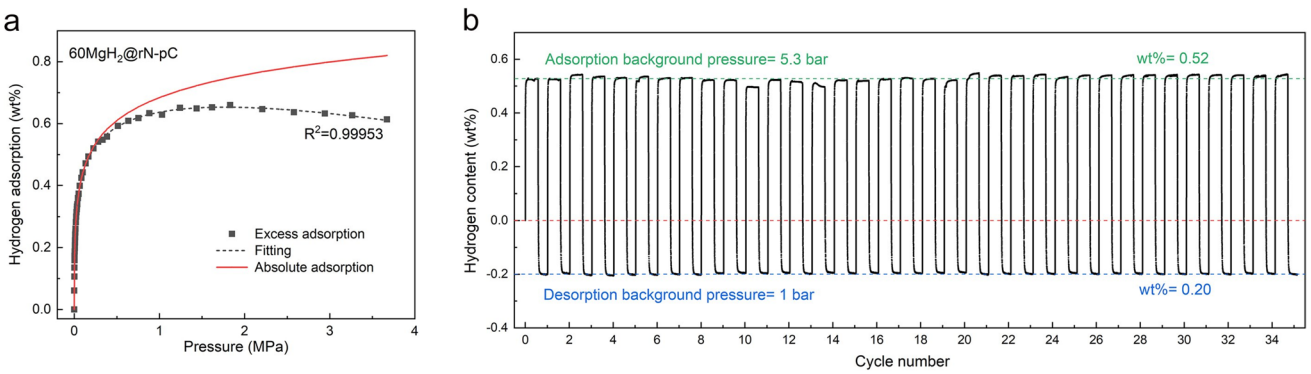

Fig. 4 Hydrogen adsorption properties of $60MgH_2$@rN-pC composite at cryogenic T. **a** Experimental and modeled H_2 excess adsorption isotherms of $60MgH_2$@rN-pC at -196 °C. **b** Cycling H_2 adsorption/desorption of $60MgH_2$@rN-pC at -196 °C

https://doi.org/10.1007/s40820-025-01931-w

Table 1 Hydrogen storage performance parameters of different Mg-carbon material nanocomposites

Carbon material	MgH_2 content (wt%)	Synthetic method	Onset desorption temperature of MgH_2 (°C)	Kinetic performance of MgH_2	H_2 pysi-/chemical sorption (wt%)	References
graphite	90	mechanical milling	280	De: 6.5 wt%/ 300 °C/30 kPa/ 20 min	–/6.5	[85]
GNS	95	mechanical milling	300	De: 1.3 wt%/ 325 °C/-/20 min	–/6.0	[86]
CNC	90	mechanical milling	245	De: 5.3 wt%/ 325 °C/-/10 min	–/5.4	[38]
CNT	90	mechanical milling	247	De: 6.0 wt%/ 300 °C/vacuum/ 3 h	–/6.5	[87]
graphene	60	nanoconfinement	250	De: 4.5 wt%/ 320 °C/1 kPa/80 min	–/4.5	[88]
CMK3	37.5	nanoconfinement	50	De: 2.1 wt%/ 300 °C/-/8 h	–/2.25	[84]
carbon aerogel	18.2	nanoconfinement	200	De: 0.9 wt%/ 300 °C/-/6 h	–/1.4	[25]
graphene	75	nanoconfinement	200	De: 2.6 wt%/ 200 °C/1 kPa/ 200 min	–/5.7	[24]
BCNTs	75	nanoconfinement	210	De: 5.8 wt%/300 °C/2 kPa/30 min	–/5.84	[89]
pCNF	60	nanoconfinement	230	De: 1.6 wt%/250 °C/1 kPa/120 min	–/4.0	[90]
MOF-derived carbon	–	–	–	–	3.25/–	[91]
MgH_2@optimized carbon	60	nanoconfinement	175	De: 3.3 wt%/300 °C/10 kPa/15 min	0.7/3.6	This work

the theoretical calculation results [79, 80]. For the fitting of 60MgH_2/rN-pC desorption curves, the parameter n was determined as ~ 1.1, which means that the reaction is controlled by particle surface reaction (first-order reaction) and the MgH_2/rN-pC interfaces serve as the active nucleation sites for Mg [81, 82]. In contrast, for the fitting of MgH_2 desorption curves, the parameter n was determined to be ~ 3.5, indicating that the inner and outer regions of hydrides are dehydrogenated simultaneously driven by high temperature and Mg nuclei form randomly inside the bulk [83]. The isothermal hydrogenation/dehydrogenation kinetics of 60MgH_2@rN-pC and MgH_2 are then measured. Figure 5c plots the isothermal desorption curves of 60MgH_2@rN-pC at different T. 60MgH_2@rN-pC releases 0.93, 2.76, 3.38, and 3.41 wt% H_2 at 250, 275, 300, and 325 °C within 30 min. At 325 °C, 60MgH_2@rN-pC can fully decompose within 5 min, while MgH_2 takes > 2 h (Fig. S18(a)). 60MgH_2@rN-pC releases almost all H_2 within 5 h at 250 °C. Even at a lower T = 225 °C, the composite can still desorb 2 wt% H_2 within 8 h, corresponding to 58.8% of the maximum H_2 storage capacity (Fig. S19). In contrast, pure MgH_2 can only release < 0.5 wt% H_2 at 300 °C within 3 h. Such an improved dehydrogenation performance confirms that the rN-pC scaffolds have a positive effect on MgH_2 dehydrogenation. The isothermal hydrogenation curves of dehydrogenated 60MgH_2@rN-pC and MgH_2 are recorded at different T for 3.2 MPa H_2 pressure (Figs. 5d and S18b). The dehydrogenated reference sample can only absorb ~ 0.72 and 4.71 wt% at 200 and 250 °C, corresponding to 10.3% and 67.3% of its maximum H_2 storage capacity, respectively. The dehydrogenated 60MgH_2@rN-pC has a fast absorption kinetics, as it can absorb 3.5 wt% H_2 at 200 °C with 50 min. Compared with Mg-carbon material composites reported in literatures, 60MgH_2@rN-pC shows relatively lower T_{onset} and enhanced desorption kinetics (Table 1). Nanoconfinement strategy has shown great ability to improve the hydrogen storage performances of Mg-based hydrogen storage materials, especially for the initial destabilization at relatively low temperature due to the interfacial catalysis [24, 84]. Besides, in this study, we investigate hydrogen adsorption ability of the supporting materials, which has the potential to address the hydrogen supply gap of Mg-based hydrogen storage materials at near-ambient temperatures. Pressure-Composition-T (PCT) absorption curves are recorded at 320, 340,

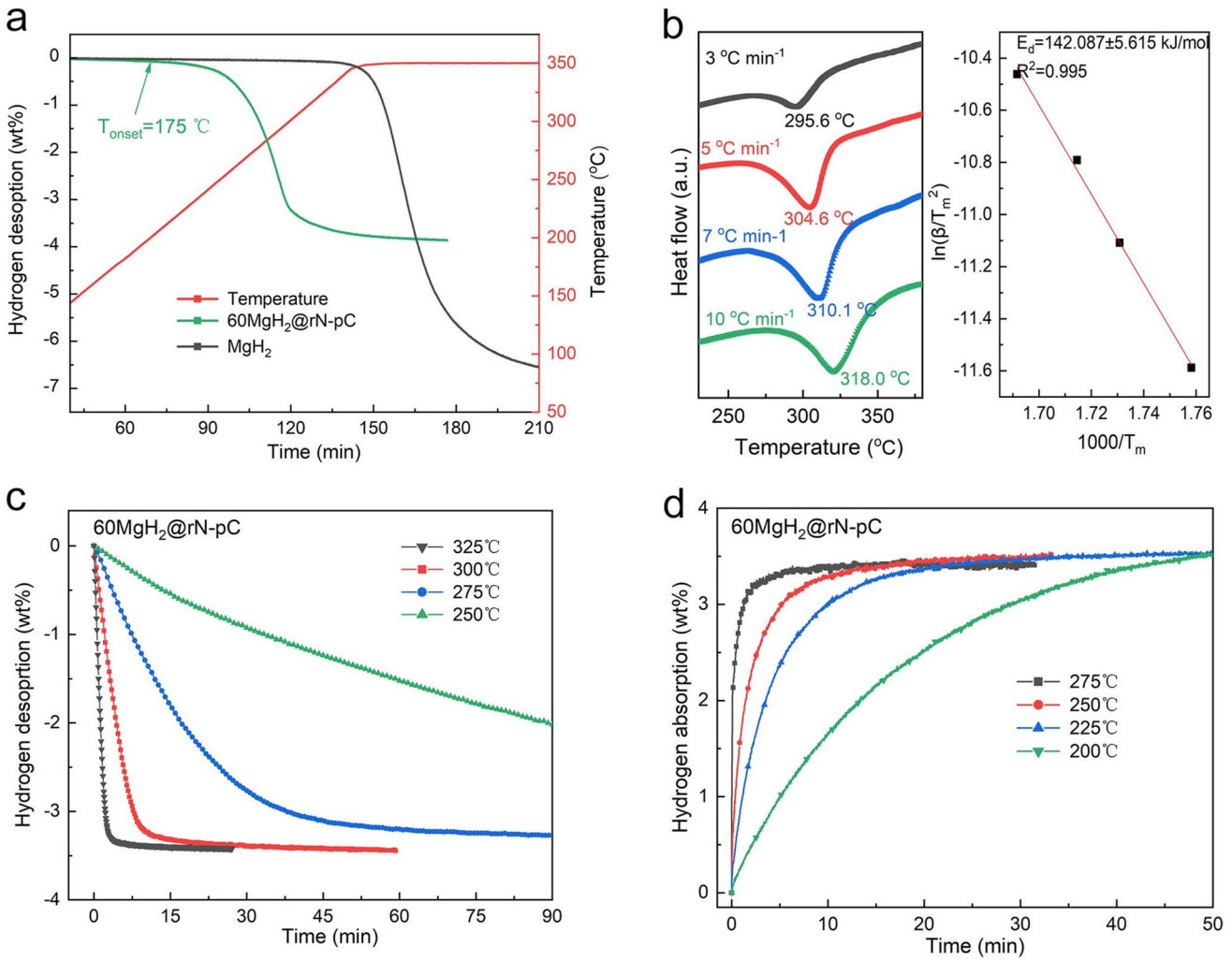

Fig. 5 Hydrogen absorption and desorption properties of $60MgH_2$@rN-pC composite at elevated T. **a** TPD of pure MgH_2 and $60MgH_2$@rN-pC. **b** DSC and corresponding Kissinger's plots of $60MgH_2$@rN-pC. **c** dehydrogenation and **d** re-hydrogenation curves of $60MgH_2$@rN-pC at different T

and 360 °C (Fig. S20a). Only one sorption pressure plateau can be observed for each isotherm, suggesting a single-step transition between Mg and MgH_2 phases during H_2 uptake. According to the van't Hoff plot (Eq. S5) [92], and fitting in Fig. S20b, the hydrogenation enthalpy for $60MgH_2$@rN-pC is determined to be ~ 67.98 ± 0.66 kJ mol^{-1} H_2, much lower than MgH_2 reported in the literatures (~ 75 kJ mol^{-1} H_2) [14], confirming that MgH_2 NPs are confined in rN-pC scaffolds, with improved thermodynamics. In order to evaluate the cycling stability of $60MgH_2$@rN-pC during the thermal de/hydrogenation processes, 10 isothermal hydrogenation/dehydrogenation cycles are performed at 275 °C. Figure S21 shows that $60MgH_2$@rN-pC has a stable H_2 sorption capacity for 10 cycles (from 3.52 wt% to 3.47 wt% for absorption and from 3.24 wt% to 3.17 wt% for desorption). Because the dehydrogenation of pure MgH_2 cannot occur at 275 °C (Fig. S18a), its cycling properties are tested at a higher T = 350 °C. Pure MgH_2 exhibits severe degradation after 10 cycles, with desorption capacity reducing from 7.3 wt% to 5.9 wt% (Fig. S22), and the kinetic performance of pure MgH_2 decays significantly after 15 cycles (Fig. S23). Reversible hydrogen absorption/desorption cycling profiles of the pure MgH_2 at 350 °C for 25 cycles and $60MgH_2$@rN-pC at 300 °C for 30 cycles also show the good stability of $60MgH_2$@rN-pC (Fig. S24), which can be ascribed to

https://doi.org/10.1007/s40820-025-01931-w

the confinement of rN-pC on MgH_2 and robust interfacial contact between host and supporting materials.

3.5 *Catalytic Mechanism of the 60MgH_2@rN-pC*

In order to investigate the mechanisms leading to improved sorption performance, we characterize the phase transformation during the thermal de/re-hydrogenation (Fig. 6a). The XRD curves of as-synthesized samples show diffraction peaks of Mg (PDF#00–004-0770) and a broad peak of C, indicating the successful loading of Mg NPs. After hydrogenation, the main peaks of MgH_2 (PDF#00–012-0697) derive from the absorption of Mg NPs [93]. A MgO (PDF#00–035-1184) peak appears ~ 42.7°, indicating amorphous impurities [94], which might react with Mg NPs during H_2 absorption. In the H_2 desorption process, MgH_2 is transformed to Mg and the peak assigned to MgO shows no change. In the whole process of H_2 absorption and desorption, there is no new phase generated besides Mg, MgH_2, MgO, with absence of additional catalytic phases.

H_2 isothermal absorption tests suggests that the thermodynamic destabilization of MgH_2 could be attributed to the "nano-size effect" of MgH_2 NPs, usually considered a key factor for thermodynamic improvement [19], since the typical crystallite sizes of MgH_2 are < 10 nm. Meanwhile, nano-confined MgH_2 NPs have a close contact with the rN-pC scaffold, introducing extra interfacial energy into the system. For MgH_2 loaded in CMK3 composites, Jia et al. calculated that the charge transfer from MgH_2 to CMK3 plays an important role in weakening Mg-H bonds [84].

Benefitting from the nondestructive synthetic method, the robust interfacial structure between MgH_2 and rN-pC was achieved and the electron transfer in the interfaces was revealed by experimental characterizations. We analyzed XPS of samples at different stages of synthesis, absorption and desorption to investigate the effect of interfaces (Fig. 6b). The three peaks at ~ 49.5, 50.5, 51.3 eV for as-synthesized MgH_2@rN-pC belong to Mg, MgO, and amorphous $Mg(OH)_2$, respectively [24]. The peaks of Mg and $Mg(OH)_2$ disappear due to the complete hydrogenation of Mg and decomposition of $Mg(OH)_2$, consistent with the XRD results of Fig. 6a. The Mg peaks reappear in the XRD patterns of samples after desorption. To evaluate the interaction between MgH_2 and rN-pC in the 60MgH_2@rN-pC composite, we synthesized pure MgH_2 and rN-pC using exactly the same methods, which were characterized as the "initial states" of the components. Then, the XPS signals of the 60MgH_2@rN-pC composite were collected to obtain the "final states" of the components. We conclude that the signal changes can be used to deduce the catalytic effects of rN-pC, which has been widely adopted in the literatures [95–97]. Compared with pure Mg, the Mg and MgH_2 peaks shift to higher binding energies in MgH_2@rN-pC. Correspondingly, the N peaks of MgH_2@rN-pC shift to lower binding energies than rN-pC (Fig. 6b). The electronegativity of N (3.07) is much higher than Mg (1.30) and C (2.54) [98]. The changes of peak positions indicate that charges transfer from MgH_2/Mg to rN-pC, consistent with the calculations of Ref. [99]. Combined with the reduced NPs size of Mg/MgH_2 and increased electronegativity of substrates, the interfacial effects impact the absorption/desorption properties of MgH_2. Moreover, XPS spectra of Mg 2*p* and N 1*s* in the 60MgH_2@rN-pC composite after 10 re/dehydrogenation cycles show the same changing tendency of peak positions as that appears in the initial cycling state, indicating that the charge transfer from MgH_2/Mg to rN-pC is stable, as well as the interfacial structures (Fig. S25).

Thus, our MgH_2 NPs are confined in a porous carbon matrix possessing H_2 adsorption capacity, besides benefiting from the catalytic activity and nanoconfinement effects of rN-pC (Fig. 7). MgH_2@rN-pC has both physical and chemical sorption properties, lowered H_2 desorption T than MgH_2, and improved cycling stability. As shown in Fig. S26 and its corresponding explanation, at RT H_2 adsorbed in rN-pC scaffolds desorbs spontaneously and ~ 0.6 wt% is released firstly. Subsequently, when the system is further heated, nano-MgH_2 in the composite continues releasing ~ 4.2 wt% H_2 in a wide T range (–196–325 °C). The maximum volumetric H_2 uptake is calculated to be ~ 43.5 g H_2 L^{-1}, considering the DFT PV (~ 0.440 cm^3 g^{-1}), skeletal density (~ 1.904 g cm^{-3}) of rN-pC. The exhaust heat from working Fuel Cell supplied by physical desorbed H_2 can be used as the heat resource for MgH_2 decomposition in the second stage. Besides, MgH_2@rN-pC can be compacted and remain a high volumetric capacity (33.4 g H_2 L^{-1}, Figs. S27 and S28). The PSD can be further optimized to achieve higher H_2 storage density.

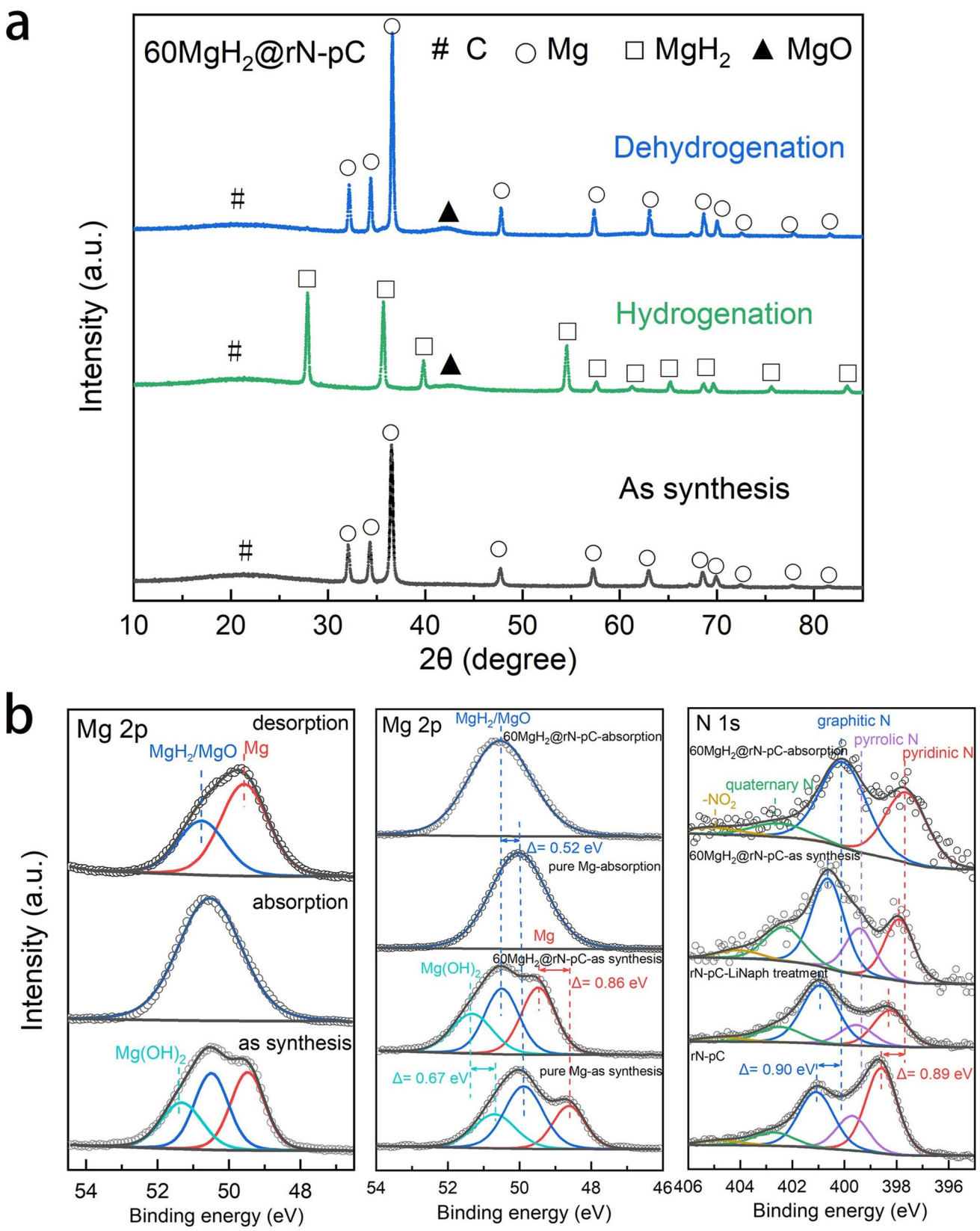

Fig. 6 Phase and electron structure change of $60MgH_2$@rN-pC composite during the absorption and desorption processes. **a** XRD patterns of $60MgH_2$@rN-pC. **b** XPS spectra of Mg 2*p* for $60MgH_2$@rN-pC (left), Mg 2*p* for pure MgH_2 and $60MgH_2$@rN-pC (middle), and N 1*s* for rN-pC and $60MgH_2$@rN-pC (right)

https://doi.org/10.1007/s40820-025-01931-w

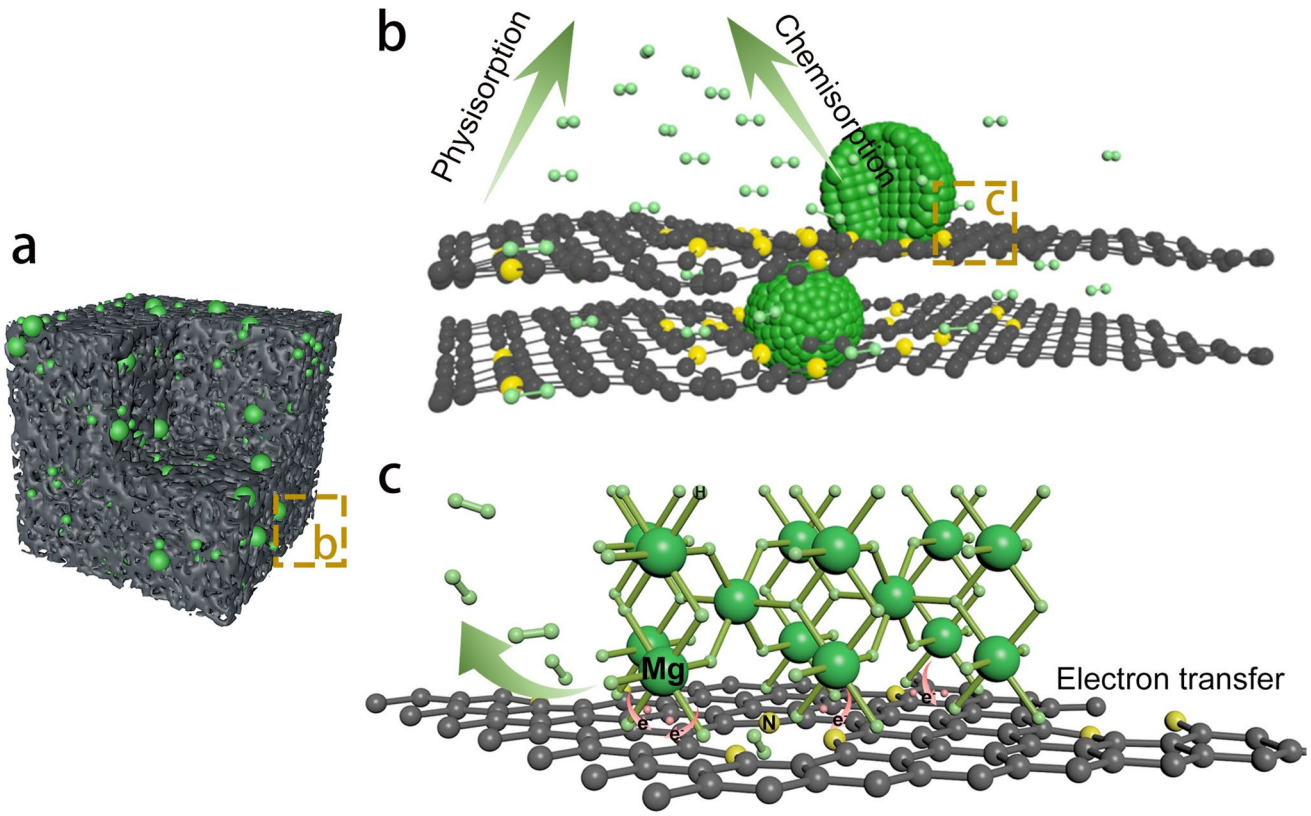

Fig. 7 Illustration of hybrid physical and chemical H_2 sorption in MgH_2@rN-pC composite

4 Conclusions

We presented a strategy to synthesize rN-pC as the supporting scaffold for nanoconfinement of Mg/MgH_2 NPs. Benefitting from the porous scaffolds and confined MgH_2 NPs, MgH_2@rN-pC shows promising H_2 storage performances with both physical adsorption and chemisorption properties. It can adsorb 0.62 wt% H_2 at -196 °C and release H_2 spontaneously with increasing T. MgH_2 NPs start to decompose at 175 °C to offer ~ 3.59 wt% H_2 continuously with a faster desorption kinetics. The Mg NPs thermodynamics can be also improved with a MgH_2 formation enthalpy ~ 68 kJ mol^{-1} H_2, mainly due to nanosize effects. For applications, the composite can be compacted to pellets with a volumetric H_2 density as high as 33.4 g L^{-1} at 500 MPa. Thanks to a strong coupling between MgH_2 NPs and rN-pC, in situ formed heterogeneous interfaces induce the charge transfer from Mg/MgH_2 to rN-pC, thereby weakening the Mg-H bonds. MgH_2@rN-pC displays an achieved cycling stability at both cryogenic (-196 °C) and elevated (275 °C) T. Our work offers a new approach for the design of H_2 storage systems with higher H_2 content through the nanoconfinement of MgH_2 using H_2 adsorbents. To develop materials that meet the US Department of Energy's (DOE's) targets [100], scaffolds are needed to improve H_2 adsorption capacity at RT and to catalyze MgH_2 to release H_2 at ambient T.

Acknowledgements This work was supported by the National Key R&D Program of China (2022YFB3803700), National Natural Science Foundation of China (52171186), Young Elite Scientists Sponsorship Program by CAST (2023QNRC001). Y. Li appreciates the support from "Zhiyuan Honor Program" for doctoral students, Shanghai Jiao Tong University. The authors acknowledge Chong Lu and Yingyan Zhao from Shanghai Jiao Tong University, and Rui Shi from Nanjing Tech University for their technical supports. The authors also acknowledge the supports from the Center of Hydrogen Science, Shanghai Jiao Tong University, and the Cambridge Graphene Centre, University of Cambridge.

Author Contributions Y. Li and J. Zou conceived and designed the study. Y. Li prepared samples. Y. Li and L. Ren carried out the hydrogen storage properties tests. Y. Li, Z. Li, and Y. Yao performed the SEM, TEM, XPS, BET, and Raman characterizations.

Y. Li, L. Ren, and Z. Li carried out the data analysis. X. Lin, W. Ding, and A. C. Ferrari helped discuss the results. Y. Li and J. Zou drew pictures and wrote the manuscript. J. Zou, A. C. Ferrari, and X. Lin managed the project and reviewed the results, data analysis, and manuscript preparation.

Declarations

Conflict of interest The authors declare no interest conflict. They have no known competing financial interests or personal relationships that could have appeared to influence the work reported in this paper. J. Z. and A. F. are editorial board members for Nano-Micro-Letters and were not involved in the editorial review or the decision to publish this article.

Supplementary Information The online version contains supplementary material available at https://doi.org/10.1007/s40820-025-01931-w.

References

1. M.D. Allendorf, V. Stavila, J.L. Snider, M. Witman, M.E. Bowden et al., Challenges to developing materials for the transport and storage of hydrogen. Nat. Chem. **14**(11), 1214–1223 (2022). https://doi.org/10.1038/s41557-022-01056-2
2. K.T. Møller, T.R. Jensen, E. Akiba, H.-W. Li, Hydrogen - A sustainable energy carrier. Prog. Nat. Sci. Mater. Int. **27**(1), 34–40 (2017). https://doi.org/10.1016/j.pnsc.2016.12.014
3. S. Chu, A. Majumdar, Opportunities and challenges for a sustainable energy future. Nature **488**(7411), 294–303 (2012). https://doi.org/10.1038/nature11475
4. M. van der Spek, C. Banet, C. Bauer, P. Gabrielli, W. Goldthorpe et al., Perspective on the hydrogen economy as a pathway to reach net-zero CO_2 emissions in Europe. Energy Environ. Sci. **15**(3), 1034–1077 (2022). https://doi.org/10.1039/D1EE02118D
5. J.P. Berro Ramirez, D. Halm, J.-C. Grandidier, S. Villalonga, F. Nony, 700 bar type IV high pressure hydrogen storage vessel burst–simulation and experimental validation. Int. J. Hydrog. Energy **40**(38), 13183–13192 (2015). https://doi.org/10.1016/j.ijhydene.2015.05.126
6. Y. Zhao, M. Gong, Y. Zhou, X. Dong, J. Shen, Thermodynamics analysis of hydrogen storage based on compressed gaseous hydrogen, liquid hydrogen and cryo-compressed hydrogen. Int. J. Hydrog. Energy **44**(31), 16833–16840 (2019). https://doi.org/10.1016/j.ijhydene.2019.04.207
7. J. Yang, A. Sudik, C. Wolverton, D.J. Siegel, High capacity hydrogen storage materials: attributes for automotive applications and techniques for materials discovery. Chem. Soc. Rev. **39**(2), 656–675 (2010). https://doi.org/10.1039/B802882F
8. S. Liu, J. Liu, X. Liu, J.-X. Shang, R. Yu et al., Non-classical hydrogen storage mechanisms other than chemisorption and physisorption. Appl. Phys. Rev. **9**(2), 021315 (2022). https://doi.org/10.1063/5.0088529
9. G.S. Walker, M. Abbas, D.M. Grant, C. Udeh, Destabilisation of magnesium hydride by germanium as a new potential multicomponent hydrogen storage system. Chem. Commun. **47**(28), 8001–8003 (2011). https://doi.org/10.1039/C0CC03425H
10. B. Bogdanović, A. Ritter, B. Spliethoff, Active MgH_2 Mg systems for reversible chemical energy storage. Angew. Chem. Int. Ed. **29**(3), 223–234 (1990). https://doi.org/10.1002/anie.199002233
11. W. Liu, Y. Mao, J. Zheng, Z. Wang, C. Shang et al., Enhancing the flotation separation of magnesite and dolomite by introducing a phosphonic acid depressant during grinding. Sep. Purif. Technol. **361**, 131412 (2025). https://doi.org/10.1016/j.seppur.2025.131412
12. P. Loganathan, G. Naidu, S. Vigneswaran, Mining valuable minerals from seawater: a critical review. Environ. Sci. Water Res. Technol. **3**(1), 37–53 (2017). https://doi.org/10.1039/c6ew00268d
13. I.P. Jain, C. Lal, A. Jain, Hydrogen storage in Mg: a most promising material. Int. J. Hydrog. Energy **35**(10), 5133–5144 (2010). https://doi.org/10.1016/j.ijhydene.2009.08.088
14. Y. Yang, X. Zhang, L. Zhang, W. Zhang, H. Liu et al., Recent advances in catalyst-modified Mg-based hydrogen storage materials. J. Mater. Sci. Technol. **163**, 182–211 (2023). https://doi.org/10.1016/j.jmst.2023.03.063
15. X. Zhang, S. Ju, C. Li, J. Hao, Y. Sun et al., Atomic reconstruction for realizing stable solar-driven reversible hydrogen storage of magnesium hydride. Nat. Commun. **15**, 2815 (2024). https://doi.org/10.1038/s41467-024-47077-y
16. X. Zhang, Y. Sun, S. Ju, J. Ye, X. Hu et al., Solar-driven reversible hydrogen storage. Adv. Mater. **35**(2), e2206946 (2023). https://doi.org/10.1002/adma.202206946
17. N.A. Niaz, I. Ahmad, W.S. Khan, S.T. Hussain, Synthesis of nanostructured Mg–Ni alloy and its hydrogen storage properties. J. Mater. Sci. Technol. **28**(5), 401–406 (2012). https://doi.org/10.1016/S1005-0302(12)60075-9
18. L. Ren, Y. Li, Z. Li, X. Lin, C. Lu et al., Boosting hydrogen storage performance of MgH_2 by oxygen vacancy-rich H-V_2O_5 nanosheet as an excited H-pump. Nano-Micro Lett. **16**(1), 160 (2024). https://doi.org/10.1007/s40820-024-01375-8

19. X. Zhang, Y. Liu, Z. Ren, X. Zhang, J. Hu et al., Realizing 6.7 wt% reversible storage of hydrogen at ambient temperature with non-confined ultrafine magnesium hydrides. Energy Environ. Sci. **14**(4), 2302–2313 (2021). https://doi.org/10.1039/D0EE03160G
20. R. Bardhan, A.M. Ruminski, A. Brand, J.J. Urban, Magnesium nanocrystal-polymer composites: a new platform for designer hydrogen storage materials. Energy Environ. Sci. **4**(12), 4882–4895 (2011). https://doi.org/10.1039/C1EE02258J
21. B. Han, Y. Jia, J. Wang, X. Xiao, L. Chen et al., The structural, energetic and dehydrogenation properties of pure and Ti-doped Mg(0001)/MgH_2(110) interfaces. J. Mater. Chem. A **11**(48), 26602–26616 (2023). https://doi.org/10.1039/d3ta06177a
22. X. Yu, Z. Tang, D. Sun, L. Ouyang, M. Zhu, Recent advances and remaining challenges of nanostructured materials for hydrogen storage applications. Prog. Mater. Sci. **88**, 1–48 (2017). https://doi.org/10.1016/j.pmatsci.2017.03.001
23. A. Schneemann, J.L. White, S. Kang, S. Jeong, L.F. Wan et al., Nanostructured metal hydrides for hydrogen storage. Chem. Rev. **118**(22), 10775–10839 (2018). https://doi.org/10.1021/acs.chemrev.8b00313
24. G. Xia, Y. Tan, X. Chen, D. Sun, Z. Guo et al., Monodisperse magnesium hydride nanoparticles uniformly self-assembled on graphene. Adv. Mater. **27**(39), 5981–5988 (2015). https://doi.org/10.1002/adma.201502005
25. T.K. Nielsen, K. Manickam, M. Hirscher, F. Besenbacher, T.R. Jensen, Confinement of MgH_2 nanoclusters within nanoporous aerogel scaffold materials. ACS Nano **3**(11), 3521–3528 (2009). https://doi.org/10.1021/nn901072w
26. M. Konarova, A. Tanksale, J. Norberto Beltramini, Q.L. Gao, Effects of nano-confinement on the hydrogen desorption properties of MgH_2. Nano Energy **2**(1), 98–104 (2013). https://doi.org/10.1016/j.nanoen.2012.07.024
27. M.A. Lillo-Ródenas, Z.X. Guo, K.F. Aguey-Zinsou, D. Cazorla-Amorós, A. Linares-Solano, Effects of different carbon materials on MgH_2 decomposition. Carbon **46**(1), 126–137 (2008). https://doi.org/10.1016/j.carbon.2007.10.033
28. Y. Fu, Z. Yu, S. Guo, Y. Li, Q. Peng et al., Catalytic effect of bamboo-like carbon nanotubes loaded with NiFe nanoparticles on hydrogen storage properties of MgH_2. Chem. Eng. J. **458**, 141337 (2023). https://doi.org/10.1016/j.cej.2023.141337
29. X. Huang, X. Xiao, W. Zhang, X. Fan, L. Zhang et al., Transition metal (Co, Ni) nanoparticles wrapped with carbon and their superior catalytic activities for the reversible hydrogen storage of magnesium hydride. Phys. Chem. Chem. Phys. **19**(5), 4019–4029 (2017). https://doi.org/10.1039/c6cp07852d
30. Z. Ma, Q. Zhang, S. Panda, W. Zhu, F. Sun et al., *In situ* catalyzed and nanoconfined magnesium hydride nanocrystals in a Ni-MOF scaffold for hydrogen storage. Sustain. Energy Fuels **4**(9), 4694–4703 (2020). https://doi.org/10.1039/D0SE00818D
31. P.E. de Jongh, R.W.P. Wagemans, T.M. Eggenhuisen, B.S. Dauvillier, P.B. Radstake et al., The preparation of carbon-supported magnesium nanoparticles using melt infiltration. Chem. Mater. **19**(24), 6052–6057 (2007). https://doi.org/10.1021/cm702205v
32. L. Ren, W. Zhu, Y. Li, X. Lin, H. Xu et al., Oxygen vacancy-rich 2D TiO_2 nanosheets: a bridge toward high stability and rapid hydrogen storage kinetics of nano-confined MgH(2). Nano-Micro Lett. **14**(1), 144 (2022). https://doi.org/10.1007/s40820-022-00891-9
33. P. Peng, H.Z.H. Jiang, S. Collins, H. Furukawa, J.R. Long et al., Long duration energy storage using hydrogen in metal–organic frameworks: opportunities and challenges. ACS Energy Lett. **9**(6), 2727–2735 (2024). https://doi.org/10.1021/acsenergylett.4c00894
34. O.K. Farha, A.Ö. Yazaydın, I. Eryazici, C.D. Malliakas, B.G. Hauser et al., *De novo* synthesis of a metal-organic framework material featuring ultrahigh surface area and gas storage capacities. Nat. Chem. **2**(11), 944–948 (2010). https://doi.org/10.1038/nchem.834
35. S.S. Han, H. Furukawa, O.M. Yaghi, W.A. Goddard III., Covalent organic frameworks as exceptional hydrogen storage materials. J. Am. Chem. Soc. **130**(35), 11580–11581 (2008). https://doi.org/10.1021/ja803247y
36. L.S. Blankenship, N. Balahmar, R. Mokaya, Oxygen-rich microporous carbons with exceptional hydrogen storage capacity. Nat. Commun. **8**, 1545 (2017). https://doi.org/10.1038/s41467-017-01633-x
37. L. Xiao, Y. Cao, W.A. Henderson, M.L. Sushko, Y. Shao et al., Hard carbon nanoparticles as high-capacity, high-stability anodic materials for Na-ion batteries. Nano Energy **19**, 279–288 (2016). https://doi.org/10.1016/j.nanoen.2015.10.034
38. Q. Zhang, Y. Huang, T. Ma, K. Li, F. Ye et al., Facile synthesis of small MgH_2 nanoparticles confined in different carbon materials for hydrogen storage. J. Alloys Compd. **825**, 153953 (2020). https://doi.org/10.1016/j.jallcom.2020.153953
39. I. Kusunoki, M. Sakai, Y. Igari, S. Ishidzuka, T. Takami et al., XPS study of nitridation of diamond and graphite with a nitrogen ion beam. Surf. Sci. **492**(3), 315–328 (2001). https://doi.org/10.1016/S0039-6028(01)01430-3
40. J.J. Nicolas, K.E. Gubbins, W.B. Streett, D.J. Tildesley, Eq. of state for the lennard-Jones fluid. Mol. Phys. **37**(5), 1429–1454 (1979). https://doi.org/10.1080/00268977900101051
41. P. Giannozzi, O. Andreussi, T. Brumme, O. Bunau, M. Buongiorno Nardelli et al., Advanced capabilities for materials modelling with quantum ESPRESSO. J. Phys. Condens. Matter **29**(46), 465901 (2017). https://doi.org/10.1088/1361-648x/aa8f79
42. J.P. Perdew, K. Burke, M. Ernzerhof, Generalized gradient approximation made simple. Phys. Rev. Lett. **77**(18), 3865–3868 (1996). https://doi.org/10.1103/physrevlett.77.3865

43. G. Kresse, D. Joubert, From ultrasoft pseudopotentials to the projector augmented-wave method. Phys. Rev. B **59**(3), 1758–1775 (1999). https://doi.org/10.1103/physrevb.59.1758
44. H.J. Monkhorst, J.D. Pack, Special points for Brillouin-zone integrations. Phys. Rev. B **13**(12), 5188–5192 (1976). https://doi.org/10.1103/physrevb.13.5188
45. Z. Xia, H. Xiao, Grand canonical ensemble modeling of electrochemical interfaces made simple. J. Chem. Theory Comput. **19**(15), 5168–5175 (2023). https://doi.org/10.1021/acs.jctc.3c00237
46. D. Bahamon, M. Khalil, A. Belabbes, Y. Alwahedi, L.F. Vega et al., A DFT study of the adsorption energy and electronic interactions of the SO_2 molecule on a CoP hydrotreating catalyst. RSC Adv. **11**(5), 2947–2957 (2021). https://doi.org/10.1039/C9RA10634K
47. H. Furukawa, K.E. Cordova, M. O'Keeffe, O.M. Yaghi, The chemistry and applications of metal-organic frameworks. Science **341**(6149), 1230444 (2013). https://doi.org/10.1126/science.1230444
48. Z. Chen, P. Li, R. Anderson, X. Wang, X. Zhang et al., Balancing volumetric and gravimetric uptake in highly porous materials for clean energy. Science **368**(6488), 297–303 (2020). https://doi.org/10.1126/science.aaz8881
49. A. Streb, M. Mazzotti, Adsorption for efficient low carbon hydrogen production: part 1: adsorption equilibrium and breakthrough studies for H2/CO_2/CH_4 on zeolite 13X. Adsorption **27**(4), 541–558 (2021). https://doi.org/10.1007/s10450-021-00306-y
50. S.Y. Sawant, K. Munusamy, R.S. Somani, M. John, B.L. Newalkar et al., Precursor suitability and pilot scale production of super activated carbon for greenhouse gas adsorption and fuel gas storage. Chem. Eng. J. **315**, 415–425 (2017). https://doi.org/10.1016/j.cej.2017.01.037
51. J. Ren, Y. Huang, H. Zhu, B. Zhang, H. Zhu et al., Recent progress on MOF-derived carbon materials for energy storage. Carbon Energy **2**(2), 176–202 (2020). https://doi.org/10.1002/cey2.44
52. C. Wang, J. Kim, J. Tang, M. Kim, H. Lim et al., New strategies for novel MOF-derived carbon materials based on nanoarchitectures. Chem **6**(1), 19–40 (2020). https://doi.org/10.1016/j.chempr.2019.09.005
53. Y. Wang, H. Liu, K. Wang, S. Song, P. Tsiakaras, 3D interconnected hierarchically porous N-doped carbon with NH_3 activation for efficient oxygen reduction reaction. Appl. Catal. B Environ. **210**, 57–66 (2017). https://doi.org/10.1016/j.apcatb.2017.03.054
54. D. Fairen-Jimenez, S.A. Moggach, M.T. Wharmby, P.A. Wright, S. Parsons et al., Opening the gate: framework flexibility in ZIF-8 explored by experiments and simulations. J. Am. Chem. Soc. **133**(23), 8900–8902 (2011). https://doi.org/10.1021/ja202154j
55. D. Liu, Y. Wu, Q. Xia, Z. Li, H. Xi, Experimental and molecular simulation studies of CO_2 adsorption on zeolitic imidazolate frameworks: ZIF-8 and amine-modified ZIF-8. Adsorption **19**(1), 25–37 (2013). https://doi.org/10.1007/s10450-012-9407-1
56. K. Li, Q. Liu, H. Cheng, M. Hu, S. Zhang, Classification and carbon structural transformation from anthracite to natural coaly graphite by XRD, Raman spectroscopy, and HRTEM. Spectrochim. Acta Part A Mol. Biomol. Spectrosc. **249**, 119286 (2021). https://doi.org/10.1016/j.saa.2020.119286
57. C. Buttersack, Modeling of type IV and V sigmoidal adsorption isotherms. Phys. Chem. Chem. Phys. **21**(10), 5614–5626 (2019). https://doi.org/10.1039/c8cp07751g
58. M. Thommes, Physical adsorption characterization of nanoporous materials. Chem. Ing. Tech. **82**(7), 1059–1073 (2010). https://doi.org/10.1002/cite.201000064
59. Q. Liang, Z. Li, Z.-H. Huang, F. Kang, Q.-H. Yang, Holey graphitic carbon nitride nanosheets with carbon vacancies for highly improved photocatalytic hydrogen production. Adv. Funct. Mater. **25**(44), 6885–6892 (2015). https://doi.org/10.1002/adfm.201503221
60. Y. Li, Y. Hu, Y. Zhao, G. Shi, L. Deng et al., An electrochemical avenue to green-luminescent graphene quantum dots as potential electron-acceptors for photovoltaics. Adv. Mater. **23**(6), 776–780 (2011). https://doi.org/10.1002/adma.201003819
61. Y. Li, Y. Zhao, H. Cheng, Y. Hu, G. Shi et al., Nitrogen-doped graphene quantum dots with oxygen-rich functional groups. J. Am. Chem. Soc. **134**(1), 15–18 (2012). https://doi.org/10.1021/ja206030c
62. K. Artyushkova, B. Kiefer, B. Halevi, A. Knop-Gericke, R. Schlogl et al., Density functional theory calculations of XPS binding energy shift for nitrogen-containing graphene-like structures. Chem. Commun. **49**(25), 2539–2541 (2013). https://doi.org/10.1039/C3CC40324F
63. A.C. Ferrari, J.C. Meyer, V. Scardaci, C. Casiraghi, M. Lazzeri et al., Raman spectrum of graphene and graphene layers. Phys. Rev. Lett. **97**(18), 187401 (2006). https://doi.org/10.1103/physrevlett.97.187401
64. A.C. Ferrari, J. Robertson, Resonant Raman spectroscopy of disordered, amorphous, and diamondlike carbon. Phys. Rev. B **64**(7), 075414 (2001). https://doi.org/10.1103/physrevb.64.075414
65. A.C. Ferrari, J. Robertson, Interpretation of raman spectra of disordered and amorphous carbon. Phys. Rev. B **61**(20), 14095–14107 (2000). https://doi.org/10.1103/physrevb.61.14095
66. Z. Shi, W. Yang, Y. Gu, T. Liao, Z. Sun, Metal-nitrogen-doped carbon materials as highly efficient catalysts: progress and rational design. Adv. Sci. **7**(15), 2001069 (2020). https://doi.org/10.1002/advs.202001069
67. N. Kostoglou, C. Koczwara, S. Stock, C. Tampaxis, G. Charalambopoulou et al., Nanoporous polymer-derived activated carbon for hydrogen adsorption and electrochemical energy storage. Chem. Eng. J. **427**, 131730 (2022). https://doi.org/10.1016/j.cej.2021.131730
68. J. Burress, M. Kraus, M. Beckner, R. Cepel, G. Suppes et al., Hydrogen storage in engineered carbon nanospaces. Nanotechnology **20**(20), 204026 (2009). https://doi.org/10.1088/0957-4484/20/20/204026

https://doi.org/10.1007/s40820-025-01931-w

69. X. Guo, J. Wang, Comparison of linearization methods for modeling the Langmuir adsorption isotherm. J. Mol. Liq. **296**, 111850 (2019). https://doi.org/10.1016/j.molliq.2019.111850
70. V.P. Ting, A.J. Ramirez-Cuesta, N. Bimbo, J.E. Sharpe, A. Noguera-Diaz et al., Direct evidence for solid-like hydrogen in a nanoporous carbon hydrogen storage material at supercritical temperatures. ACS Nano **9**(8), 8249–8254 (2015). https://doi.org/10.1021/acsnano.5b02623
71. I. López-Corral, J. de Celis, A. Juan, B. Irigoyen, DFT study of H_2 adsorption on Pd-decorated single walled carbon nanotubes with C-vacancies. Int. J. Hydrog. Energy **37**(13), 10156–10164 (2012). https://doi.org/10.1016/j.ijhydene.2011.12.073
72. R. Muhammad, Y. Shuai, H.-P. Tan, First-principles study on hydrogen adsorption on nitrogen doped graphene. Phys. E Low Dimens. Syst. Nanostruct. **88**, 115–124 (2017). https://doi.org/10.1016/j.physe.2016.12.012
73. G. Sethia, A. Sayari, Activated carbon with optimum pore size distribution for hydrogen storage. Carbon **99**, 289–294 (2016). https://doi.org/10.1016/j.carbon.2015.12.032
74. J. Li, R. Zou, Y. Cui, G. Lei, Z. Li et al., *In situ* formed $MgTi_2O_4$ from MgO improving the cycling stability of MgH_2. Chem. Eng. J. **470**, 144259 (2023). https://doi.org/10.1016/j.cej.2023.144259
75. L.S. Blankenship, R. Mokaya, Modulating the porosity of carbons for improved adsorption of hydrogen, carbon dioxide, and methane: a review. Mater. Adv. **3**(4), 1905–1930 (2022). https://doi.org/10.1039/D1MA00911G
76. L. Borchardt, D. Leistenschneider, J. Haase, M. Dvoyashkin, Revising the concept of pore hierarchy for ionic transport in carbon materials for supercapacitors. Adv. Energy Mater. **8**(24), 1800892 (2018). https://doi.org/10.1002/aenm.201800892
77. R.L. Blaine, H.E. Kissinger, Homer Kissinger and the Kissinger eq. Thermochim. Acta **540**, 1–6 (2012). https://doi.org/10.1016/j.tca.2012.04.008
78. F. Jensen, Activation energies and the Arrhenius Eq. Qual. Reliab. Eng. Int. **1**(1), 13–17 (1985). https://doi.org/10.1002/qre.4680010104
79. E.M. Kumar, A. Rajkamal, R. Thapa, Screening based approach and dehydrogenation kinetics for MgH_2: guide to find suitable dopant using first-principles approach. Sci. Rep. **7**(1), 15550 (2017). https://doi.org/10.1038/s41598-017-15694-x
80. S. Dong, C. Li, J. Wang, H. Liu, Z. Ding et al., The "burst effect" of hydrogen desorption in MgH_2 dehydrogenation. J. Mater. Chem. A **10**(42), 22363–22372 (2022). https://doi.org/10.1039/D2TA06458H
81. A.S. Awad, E. El-Asmar, T. Tayeh, F. Mauvy, M. Nakhl et al., Effect of carbons (G and CFs), TM (Ni, Fe and Al) and oxides (Nb_2O_5 and V_2O_5) on hydrogen generation from ball milled Mg-based hydrolysis reaction for fuel cell. Energy **95**, 175–186 (2016). https://doi.org/10.1016/j.energy.2015.12.004
82. E. Alasmar, A.S. Awad, D. Hachem, T. Tayeh, M. Nakhl et al., Hydrogen generation from Nd-Ni-Mg system by hydrolysis reaction. J. Alloys Compd. **740**, 52–60 (2018). https://doi.org/10.1016/j.jallcom.2017.12.305
83. T. Huang, C. Zhou, Surface diffusion-controlled jonhson–mehl–avrami–Kolmogorov model for hydrogenation of Mg-based alloys. J. Phys. Chem. C **127**(28), 13900–13910 (2023). https://doi.org/10.1021/acs.jpcc.3c02650
84. Y. Jia, C. Sun, L. Cheng, M. Abdul Wahab, J. Cui et al., Destabilization of Mg–H bonding through nano-interfacial confinement by unsaturated carbon for hydrogen desorption from MgH_2. Phys. Chem. Chem. Phys. **15**(16), 5814–5820 (2013). https://doi.org/10.1039/C3CP50515D
85. V. Fuster, F.J. Castro, H. Troiani, G. Urretavizcaya, Characterization of graphite catalytic effect in reactively ball-milled MgH_2–C and Mg–C composites. Int. J. Hydrog. Energy **36**(15), 9051–9061 (2011). https://doi.org/10.1016/j.ijhydene.2011.04.153
86. Q. Zhang, Y. Xu, Y. Wang, H. Zhang, Y. Wang et al., Enhanced hydrogen storage performance of MgH_2 Ni2P/graphene nanosheets. Int. J. Hydrog. Energy **41**(38), 17000–17007 (2016). https://doi.org/10.1016/j.ijhydene.2016.07.133
87. S. Gao, X. Wang, H. Liu, T. He, Y. Wang et al., Effects of nano-composites (FeB, FeB/CNTs) on hydrogen storage properties of MgH_2. J. Power. Sources **438**, 227006 (2019). https://doi.org/10.1016/j.jpowsour.2019.227006
88. Y. Huang, G. Xia, J. Chen, B. Zhang, Q. Li et al., One-step uniform growth of magnesium hydride nanoparticles on graphene. Prog. Nat. Sci. Mater. Int. **27**(1), 81–87 (2017). https://doi.org/10.1016/j.pnsc.2016.12.015
89. M. Liu, S. Zhao, X. Xiao, M. Chen, C. Sun et al., Novel 1D carbon nanotubes uniformly wrapped nanoscale MgH_2 for efficient hydrogen storage cycling performances with extreme high gravimetric and volumetric capacities. Nano Energy **61**, 540–549 (2019). https://doi.org/10.1016/j.nanoen.2019.04.094
90. L. Ren, W. Zhu, Q. Zhang, C. Lu, F. Sun et al., MgH_2 confinement in MOF-derived N-doped porous carbon nanofibers for enhanced hydrogen storage. Chem. Eng. J. **434**, 134701 (2022). https://doi.org/10.1016/j.cej.2022.134701
91. S.J. Yang, T. Kim, J.H. Im, Y.S. Kim, K. Lee et al., MOF-derived hierarchically porous carbon with exceptional porosity and hydrogen storage capacity. Chem. Mater. **24**(3), 464–470 (2012). https://doi.org/10.1021/cm202554j
92. J.F. Stampfer Jr., C.E. Holley Jr., J.F. Suttle, The magnesium-hydrogen System[1-3]. J. Am. Chem. Soc. **82**(14), 3504–3508 (1960). https://doi.org/10.1021/ja01499a006
93. M.S. El-Eskandarany, Metallic glassy Ti_2Ni grain-growth inhibitor powder for enhancing the hydrogenation/dehydrogenation kinetics of MgH_2. RSC Adv. **9**(2), 1036–1046 (2019). https://doi.org/10.1039/C8RA08200F
94. H. Liang, D. Chen, D. Thiry, W. Li, M. Chen et al., Efficient hydrogen storage with the combination of metal Mg and porous nanostructured material. Int. J. Hydrogen Energy

44(31), 16824–16832 (2019). https://doi.org/10.1016/j.ijhydene.2019.04.212

95. Y. Li, L. Ren, Y. Yao, Y. Zhao, H. Xu et al., A single-atom interface engineering strategy to promote hydrogen sorption performances of magnesium hydride. Adv. Funct. Mater. **35**(13), 2417915 (2025). https://doi.org/10.1002/adfm.202417915
96. Y. Teng, Y. Zhang, X. Xie, J. Yao, Z. Zhang et al., Interfacial electron transfer in PbI_2@single-walled carbon nanotube van der Waals heterostructures for high-stability self-powered photodetectors. J. Am. Chem. Soc. **146**(9), 6231–6239 (2024). https://doi.org/10.1021/jacs.3c14188
97. Y. Xia, L. Wang, G. Gao, T. Mao, Z. Wang et al., Constructed Mott-schottky heterostructure catalyst to trigger interface disturbance and manipulate redox kinetics in Li-O_2 battery. Nano-Micro Lett. **16**(1), 258 (2024). https://doi.org/10.1007/s40820-024-01476-4
98. L.C. Allen, Electronegativity is the average one-electron energy of the valence-shell electrons in ground-state free atoms. J. Am. Chem. Soc. **111**(25), 9003–9014 (1989). https://doi.org/10.1021/ja00207a003
99. D. He, Y. Wang, C. Wu, Q. Li, W. Ding et al., Enhanced hydrogen desorption properties of magnesium hydride by coupling non-metal doping and nano-confinement. Appl. Phys. Lett. **107**(24), 243907 (2015). https://doi.org/10.1063/1.4938245
100. U. D. O. Energy, Targets for onboard hydrogen storage systems for light-duty vehicles, (2009).

https://doi.org/10.1007/s40820-025-01931-w